

# Exposure of Arctic coastal settlements to coastal erosion and permafrost warming

Rodrigue Tanguy<sup>1</sup>, Annett Bartsch<sup>1</sup>, Ingmar Nitze<sup>2</sup>, Anna Irrgang<sup>2</sup>, Pia Petzold<sup>2</sup>, Barbara Widhalm<sup>1</sup>, Clemens von Baeckmann<sup>1</sup>, Julia Boike<sup>2</sup>, Julia Martin<sup>2</sup>, Aleksandra Efimova<sup>1</sup>, Gonçalo Vieira<sup>3</sup>, Birgit Heim<sup>2</sup>, Mareike Wieczorek<sup>2</sup>, Guido Grosse<sup>2</sup>, Dorothee Ehrich<sup>4</sup>

<sup>1</sup>Austrian Polar Research Institute - b.geos GmbH, Korneuburg, Austria

<sup>2</sup>Alfred Wegener Institute for Polar and Marine Research, Potsdam, Germany

<sup>3</sup>Centre of Geographical Studies, TERRA Associated Laboratory, Institute of Geography and Spatial

Planning, University of Lisbon, Lisbon, Portugal

<sup>4</sup>UiT The Arctic University of Norway, Tromsø, Norway

## Key Points:

- By 2100, nearly one quarter of Arctic coastal settlements will be impacted by coastal erosion
- Permafrost warming will affect 65 percent of present infrastructures, potentially enhancing ground subsidence
- Immediate adaptation strategies are essential to protect Arctic and communities and infrastructure from these environmental changes

---

Corresponding author: Rodrigue Tanguy, [rodrigue.tanguy@bgeos.com](mailto:rodrigue.tanguy@bgeos.com)

## Abstract

This study assesses the vulnerability of Arctic coastal settlements and infrastructures to coastal erosion and permafrost warming. We enhanced the Arctic Coastal Infrastructure dataset (SACHI) to include road types, airstrips, and artificial water reservoirs. Analysis of coastline change rates from 2000-2020, permafrost ground temperature and active layer thickness changes from the ESA Permafrost Climate Change Initiative identified at-risk settlements for 2030, 2050, and 2100. Our study incorporates a thorough validation process for each dataset utilized, ensuring the verification and accuracy of the data. Our findings are concerning: by 2100, 23% of Arctic coastal settlements will be impacted by coastal erosion. Based on linear trends, permafrost ground temperature will rise by 8°C and active layer thickness will increase by 0.9 m. 65% of all present infrastructures/settlements will be affected by permafrost warming between 5-15°C and 35% from active layer thickening of 1-5 meter. This is the first study to identify settlements at risk from coastal erosion and warming permafrost along Arctic and permafrost-dominated coasts at a regional scale for the northern hemisphere. We provide an estimation of the total number of coastal communities and associated infrastructures being directly endangered by coastal erosion until 2100. Our results highlight that adaptation to current and future environmental changes is needed now in order to counteract a deterioration of living conditions in permafrost coastal settlements.

## Plain Language Summary

This study examines the risks to Arctic coastal areas and infrastructure, such as roads and buildings, from increasing coastal erosion and permafrost warming. Analyzing coastline changes, permafrost temperatures, and the thickness of the thawing layer from 2000 to 2020, we identified the areas most at risk by 2030, 2050, and 2100. Our research finds that by 2100, about 23% of Arctic coastal settlements may face infrastructure damage due to coastal erosion. Additionally, permafrost is likely to warm by 8°C, and its top thawing layer could thicken by 0.9 meters, potentially affecting 65% of existing infrastructure and settlements with enhanced ground instability. This is the first large-scale study assessing coastal erosion and permafrost warming risks along Arctic and permafrost-rich coasts across the northern hemisphere. We estimate that a significant number of coastal communities and their infrastructures are at risk until 2100. These findings highlight the urgent need for adaptation strategies to mitigate environmental changes and protect the living conditions in Arctic permafrost coastal areas.

## 1 Introduction

In a context of recent and rapid warming of the Arctic region, oceanic and terrestrial environments are experiencing rapid changes. Modeled projections are confirming a significant increase of these changes by 2100 (IPCC, 2022), impacting the biosphere and Arctic and permafrost living communities. A major change occurring within the Arctic Ocean is the rapid decline of sea-ice extent and thickness due to global warming (Stroeve & Notz, 2018; Meredith et al., 2019). The summer sea-ice extent is expected to decline by 12.6% per decade and the open-water season to lengthen from 63 to 90 days by 2100 (A. Crawford et al., 2021), increasing the exposure time of the Arctic coast to dynamic marine conditions and storm impacts (Overeem et al., 2011; A. D. Crawford et al., 2022). By 2100, the global sea level is predicted to rise between 0.3 to 1.1 meters (Oppenheimer et al., 2019) due to oceanic thermal expansion, glaciers, and ice-sheets melting (Oppenheimer et al., 2019; Box et al., 2022), which can be also observed in the Arctic Ocean (Rose et al., 2019). Rising relative and absolute sea levels in combination with increasingly severe storms, are especially impacting communities being placed in low-lying coastal areas and exposed to coastal erosion and flooding events (Irrgang et al., 2022).



Terrestrial permafrost is degrading in response to increasing mean air temperature which transfers to rising ground temperatures and more precipitation (Vasiliev et al., 2020; Smith et al., 2022). In the Northern Hemisphere (NH), permafrost ground temperatures (GT) have been increasing on average by about 1°C since 1997 (Bartsch et al., 2023). Its warming contributes to the deepening of the active layer thickness (ALT) enhancing thermokarst processes where ground-ice thawing generates lake and thaw-pond formation, lake drainage, ground subsidence and shoreline destabilization (Smith et al., 2022; Hjort et al., 2022). At the interface between land and sea, the permafrost coastline and local communities are subject to various pressures. Arctic permafrost coasts are among the fastest eroding coasts of the globe and are registering extreme erosion rates locally exceeding 40 m/yr (Malenfant et al., 2022). The average pan-arctic coastal retreat rate was estimated at 0.5 m/yr from Lantuit et al. (2012) and is expected to double before the end of the century (Nielsen et al., 2022). Erosion is a natural process but was observed to accelerate in various regions during last decades (B. M. Jones et al., 2018; Irrgang et al., 2018; Isaev et al., 2019; Whalen et al., 2022; Tanguy, Whalen, Prates, & Vieira, 2023). High retreat rates are mainly occurring where unlithified but ice-bound tundra cliffs are exposed to waves during the sea-ice free season. The Beaufort coast is experiencing one of highest mean retreat rates of the Arctic with 1.1 m/yr (Overduin et al., 2014) and the highest rates are related to block failures generated by the combination of ground-ice thawing and sapping from wave action at the cliff-base (Cunliffe et al., 2019; Thomas et al., 2020). Low-lying areas are especially vulnerable to coastal erosion and flooding, which are important issues for coastal communities since they are impacting livelihoods and infrastructure (Radosavljevic et al., 2016; Tanguy, Whalen, Prates, Pina, et al., 2023). Various coastal settlements have been majorly impacted by coastal erosion, storm surges and flooding such as Shishmaref in Alaska and Tuktoyaktuk in Canada (Marino & Lazrus, 2015; Whalen et al., 2022). Under such conditions, the stability of roads, airstrips, buildings, oil tanks and pipelines is becoming an important economic and environmental issue and poses engineering challenges for coastal communities (Buzard et al., 2021; Hjort et al., 2022; D. A. Streletskiy et al., 2019a).

Satellite data can be potentially used to implement a circumarctic monitoring scheme. The Sentinel-1/2 derived Arctic Coastal Human Impact dataset (SACHI; Bartsch et al. (2021)) shows increasing human presence and industrial activity linked to oil/gas exploitation and mining along the Arctic. This dataset considered three types of human impact as visible from space: linear transport infrastructure (roads and railways), buildings and other constructions (e.g. bridges), and other impacted areas (gravel pads, open pit mining areas, etc.) and was limited to a 100 km fringe from the Arctic and permafrost coastline. In the latter classification, airstrips were not distinguished individually and were included in the "other impacted area" class, and different road construction types (gravel versus tarmac) were not considered. Initial analyses showed the potential of satellite data to separate road types (Bartsch, Pointner, et al., 2020). Artificial water bodies were also not included although water surfaces can be easily detected with satellite data. These features are built for water supply but also from the oil and mining industry, potentially promoting contaminants accumulations and local pollution issues (Glotov et al., 2018). The classification of different types of road, airstrips and the addition of water reservoirs is essential not only for a better characterization of human impact zones, but also for potential risk assessments including the socio-economic values of the various infrastructures.

Permafrost coastline evolution is commonly assessed using historical aerial photography combined with high-resolution satellite imagery, or airborne data. The variety of scales, investigated time periods and study sites extends makes it difficult to compare regions and to get a comprehensive picture of pan-arctic coastal dynamics. The Arctic Coastal Dynamic Database (ACD) from Lantuit et al. (2012) provided a first compilation of shoreline change data, filling observation gaps with expert estimates. Landsat satellite imagery is a valuable data source due to its free availability, and large spatio-temporal coverage. Widely used for land-cover changes studies, it can also be used to assess coastline evolution. However, the 30 m spatial resolution limits the detection of small changes (Xu, 2018). Nitze et al. (2017)

provided an efficient machine-learning based method using Landsat-trends to detect lake dynamics at a regional scale. It builds on a probability measure for land to water and water to land conversion. Bartsch, Ley, et al. (2020) demonstrate the utility of an adaptation of this approach for coastline change identification.

Coastal infrastructures can be threatened by coastal erosion, moreover, GT and ALT conditions are also changing within the last decades, which contribute to additional potential infrastructure damages via ground subsidence and hydrological changes. Time series of mean annual GT and ALT are available from a combination of satellite data (land-surface temperature) and reanalyses data through modelling at approximately 1 km nominal resolution for 1997 to 2019 (Obu et al., 2021a, 2021b; Westermann et al., 2015). Increasing temperatures have been identified based on these datasets for the Northern Hemisphere (Bartsch et al., 2023), and are pronounced along permafrost coastal regions (Miner et al., 2022) including sites with comparably high coastal erosion rates (Bartsch, Ley, et al., 2020).

In this study we (1) provide an update of the SACHI pan-arctic infrastructures dataset using a new classification including road types, airstrips and artificial water reservoirs, (2) estimate coastal dynamics and erosion rates along coastal settlements based on land-cover change detection using the approach of Bartsch, Ley, et al. (2020) for the coastline change assessment, (3) identify coastal settlements exposed to the risk of coastal erosion and/or permafrost GT and ALT increase over short-, mid- and long-term periods (2030, 2050, 2100), and (4) evaluate the accuracy of these different satellite derived datasets using various very-high resolution and in-situ validation data at key sites along permafrost-dominated coast.

## 2 Study Area

Our analysis is covering the coast bordering the Arctic Ocean, in addition, we extended our study area to the south, to include the largest part of NH permafrost-dominated coastlines. The infrastructures analysis considers the similar extent as the SACHI dataset, defined as a 100 km buffer along Arctic and permafrost-dominated coasts, allowing to include settlements located within estuaries and deltas. The SACHI dataset extents from northwest Alaska through the northern coast of the American continent including the Canadian Arctic Archipelago to the Hudson Bay until Newfoundland. Greenland, Svalbard and East Scandinavia are included as well as the entire Russian coast (Fig. 1). This area represents 62 000 km<sup>2</sup> and includes a total of 408 settlements, with 292 being directly located at the coast. These settlements are defined as areas with concentrated infrastructure, like for example hamlets, towns, mining or military bases.

The coastline dynamics dataset extent is more restricted due to the lack of sufficient Landsat acquisitions and due to the large presence of sea-ice along highest coastal latitudes (e.g Canadian Archipelago), making the analysis inaccurate. The dataset excludes western Scandinavia, northern parts of the Canadian Arctic Archipelago, the Hudson Bay and Newfoundland (Fig. 1).

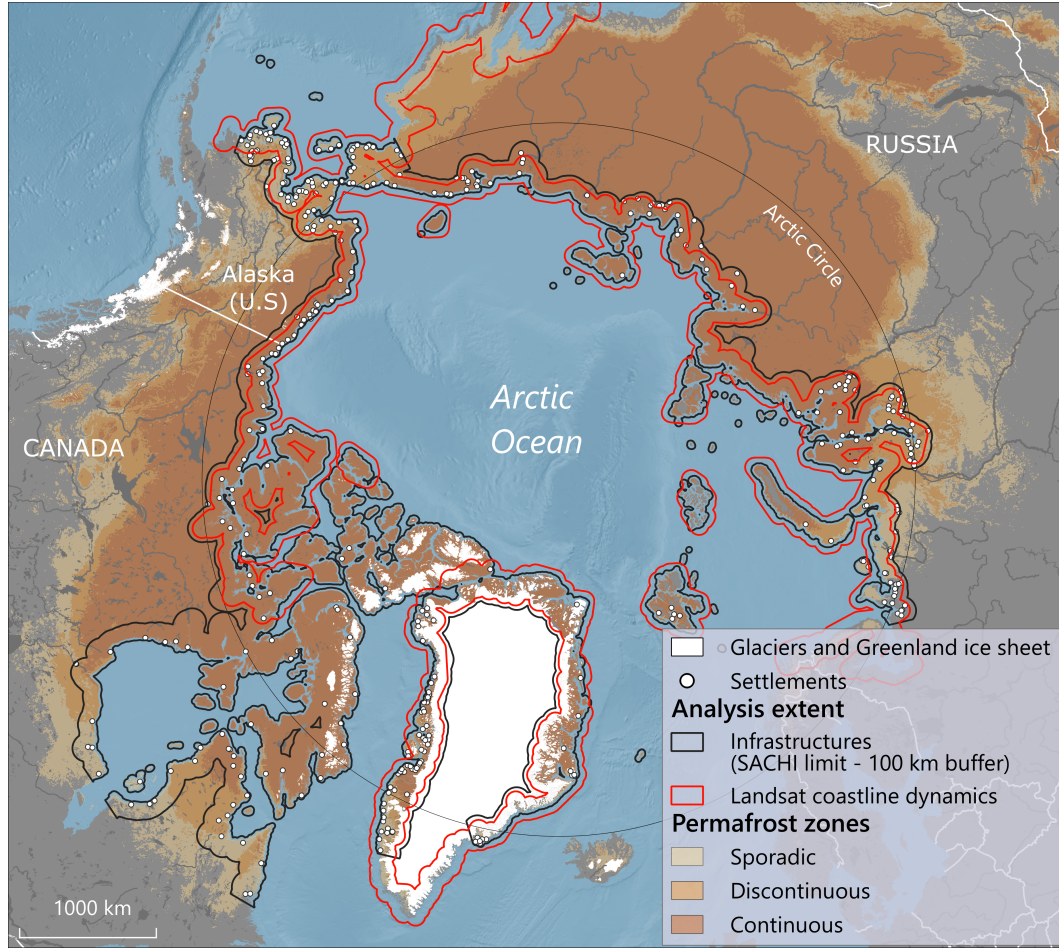


**Figure 1.** Overview of analysed areas. The SACHI 100 km coastal zone (black; Bartsch et al. (2021)) with included settlements (white dots) and the extent of Landsat derived coastal dynamics (red). Permafrost zones are derived from Obu et al. (2021c) and background data from GSHHG and CleanTOPO 2

### 3 Data

#### 3.1 Infrastructure dataset: Sentinel-1/2

As for the first version of the SACHI dataset, this work uses a combination of Sentinel-1 (Synthetic Aperture Radar-SAR) and Sentinel-2 (multi-spectral-optical) for the detection of human footprints along Arctic and permafrost-dominated coasts, using Gradient Boosting Machine (GBM) and Deep Learning (Keras) methods. In total 2424 granules at 100 by 100 km extent acquired from 2016 to 2020 were used in the analysis. More details on data and framework are described in Bartsch, Pointner, et al. (2020) and Bartsch et al. (2021).

#### 3.2 Coastline dynamics dataset: Landsat-7/8

Coastline change rates were retrieved using satellite data from Landsat 7 and 8 data from the TM, ETM+ and OLI sensors, also covering NH permafrost-dominated coasts. The study period ranges between 2000 and 2020 in order to represent recent coastal changes, also due to sparse data acquisition before 2000 in Siberia and Northern Alaska. Some areas were excluded from the analysis due to tiles with sparse availability or noise issues. We applied

a filtering of images available between July and August with cloud covers below 70%. The used Landsat bands have a spatial resolution of 30 m: Blue, Green, Red, Near-Infrared (NIR), Shortwave Infrared 1 (SWIR1), and Shortwave Infrared 2 (SWIR2).

### 3.3 Permafrost ground temperature and active layer thickness

Permafrost trends for GT and ALT were built based on a subset for the 2000-2020 period using the datasets from the European Space Agency's (ESA) climate change initiative (CCI) permafrost project (Obu et al., 2021b, 2021a). The datasets are based on MODIS land surface temperature merged with down-scaled and bias-corrected ERA5 reanalysis near-surface air temperature data. The outputs consists of raster layers with approximately 1 km nominal spatial resolution. This dataset was previously combined with the SACHI dataset from Bartsch et al. (2021). Comprehensive validation information is available within the documentation (Heim et al., 2021), but specifically active layer thickness data availability was limited and coastal region specific evaluation is unavailable.

### 3.4 Validation data

The updated SACHI dataset went through a validation process with comparison against very-high resolution imagery such as Unmanned Aerial Vehicle (UAV) orthomosaics and Pléiades© satellites scenes (CNES/Airbus), acquired at eight validation sites along the Beaufort, Yukon, Amundsen Gulf coasts (Komakuk, Tuktoyaktuk, Paulatuk, Bathurst, Cape Parry, Paulatuk, Sachs Harbour and Ulukhaktok; see Fig. 2). Vectorized infrastructure data from field survey and aerial imagery were used in Greenland settlements, in Svalbard, and in Russia (Ehrich et al., 2019; Ingeman-Nielsen & Vakulenko, 2018). In total, 21 locations were used for infrastructure validation. A dedicated survey of road types was carried out in Longyearbyen, Barentsburg and Pyramiden, in Svalbard, in 2021.

Coastline change rates were validated at four sites using local measurements derived from aerial imagery, or very-high resolution (VHR) satellite imagery corresponding to a time-period between 2000 and 2020. The validation imagery have a spatial resolution ranging from 0.5 to 1.25 m. The coastlines were manually digitized and their positional accuracy was calculated based on their spatial resolution and georeferencing quality, in order to evaluate the coastline change rate uncertainty (Table 4).

Finally, the ESA Permafrost Climate Change Initiative (Permafrost\_cci) Active Layer Thickness product was compared to in-situ thaw depth data: T-MOSAiC 2021-myThaw (Martin et al., 2023) which provided seasonal thaw depth measured along transects distributed in eight Arctic sites, located in Siberia, Svalbard, Alaska, Greenland and Canada (Boike et al., 2021). Additional records have been compiled based on the Circumarctic Active Layer Measurements (CALM; D. Streletskiy and Shiklomanov (2021)) network as part of the Permafrost\_cci documentation (Heim et al., 2021). The validation site are represented in Fig. 2.

**Table 1.** Validation data overview. For sites location, see Fig. 2

| Feature                   | Data source type                             | Data format | Site  | Region  | Time period | n° sites | Source   |
|---------------------------|--|-------------|---|---|-------------|----------|--|
| <b>Infrastructure</b>     | UAV orthomosaic                              | raster      | Tuktoyaktuk, Paulatuk, Komakuk  | Yukon, Canadian Beaufort Sea coast, Amundsen Gulf   | 2018, 2019  | 3        | IGOT-ULisboa   |
|                           | Pléiades scenes (multispectral-pausharpened) | raster      | Tuktoyaktuk, Paulatuk, Ulukhaktok, Sachs Harbour, Cape Parry, Barthurst                         | Canadian Beaufort Sea coast, Amundsen Gulf  | 2020, 2021  | 6        | Pléiades© CNES, 2020, 2021, Airbus DS  |
|                           | Quickbird & WorldView II                     | shapefile   | Chesterfield Inlet  | Nunavut (Canada)  | 2019        | 1        | Ehrich et al. (2019)   |
|                           | Quickbird & WorldView II                     | shapefile   | Gas-Sale, Katanga   | Taimyr, Yamal (Russia)  | 2019        | 2        | Ehrich et al. (2019)   |
|                           | Quickbird & WorldView II                     | shapefile   | Arqsuk, Nuqsut, Unalakleet, Brevig Mission, Prudhoe Bay   | Alaska  | 2019        | 5        | Ehrich et al. (2019)   |
|                           | cadastral                                    | shapefile   | Inlissat, Kangerlussuaq, Oqaasut, Qeqertarsuaq  | Western Greenland   | 2018        | 4        | Ingeman-Nielsen and Vakulenko (2018)   |
|                           | cadastral                                    | shapefile   | Longyearbyen  | Svalbard  | 2018        | 1        | Lu et al. (2018)   |
|                           | road type survey                             | database    | Longyearbyen  | Svalbard  | 2019        | 1        | this study   |
|                           | Maxar WV2 (pausharpened)                     | shapefile   | Barter Island   | Alaskan Beaufort Sea coast  | 2000-2020   | 1        | Gibbs et al. (2020)  |
|                           | Aerial photos (panchromatic)                 | shapefile   | Mackenzie Delta   | Canadian Beaufort Sea coast   | 2000-2018   | -        | Solomon (2005)   |
| <b>Coastline dynamics</b> | Pléiades (multispectral-pausharpened)        | shapefile   | Point Lonely Air Station  | Alaskan North Slope   | 2000-2018   | 1        | Pléiades© CNES, 2018, Airbus DS  |
|                           | Maxar Ikonos (panchromatic)                  | shapefile   | Newtok  | Bethel Census (Alaska)  | 2005-2019   | 1        | Google Earth©  |
|                           | Pléiades (multispectral-pausharpened)        | shapefile   | Newtok  | Bethel Census (Alaska)  | 2005-2019   | 1        | Google Earth©  |
|                           | Pléiades (multispectral-pausharpened)        | shapefile   | Newtok  | Bethel Census (Alaska)  | 2005-2019   | 1        | Google Earth©  |
| <b>ALT</b>                | in-situ ALT measurements                     | database    | Bayeta (2), Kevo Waisejaeggi, Samoylov, Toolik Lake, Siksik Creek, Cambridge Bay, Zakenberg (2) | Alaskan North Slope, Canada, Greenland, Svalbard, Nordic Region, Central Siberia, Nunavut | 2021        | 8        | T-MOSAIC MyThaw Bolke et al. (2021)<br>CALM D. Streletsky and Shiklomanov (2021) |





**Figure 2.** Validation sites for infrastructures, coastline change rates and active layer thickness. Background data: GSHHG; Cleantopo2 (ocean bottom).

## 4 Methods

### 4.1 General approach

This work provides an update of the published Sentinel-1/2 derived Arctic Coastal Human Impact dataset (SACHI) with the inclusion of new classes such as asphalt, dirt and undefined roads, airstrips and artificial water reservoirs, using a combination of Deep Learning (DL) and Machine Learning (ML) methods. Areas of erosion and accretion are derived from Landsat change probabilities for the period 2000-2020. The retrieved coastline change rates were combined with the infrastructure dataset in order to evaluate settlements exposure to coastal erosion for short-, mid- and long-term (2030, 2050, 2100). In addition, GT and ALT trends are considered for the evaluation of permafrost thaw exposure. Each dataset was compared to validation data described in Table 1, in order to evaluate their accuracy. The SACHI update considers settlements and infrastructure within the 100 km buffer zone of the coastline. New settlements and associated information was added to the settlement database. The fusion of coastline change rates and permafrost properties with the infrastructure dataset allows for the vulnerability assessment of coastal settlements. The overall workflow is shown in Fig. 3.

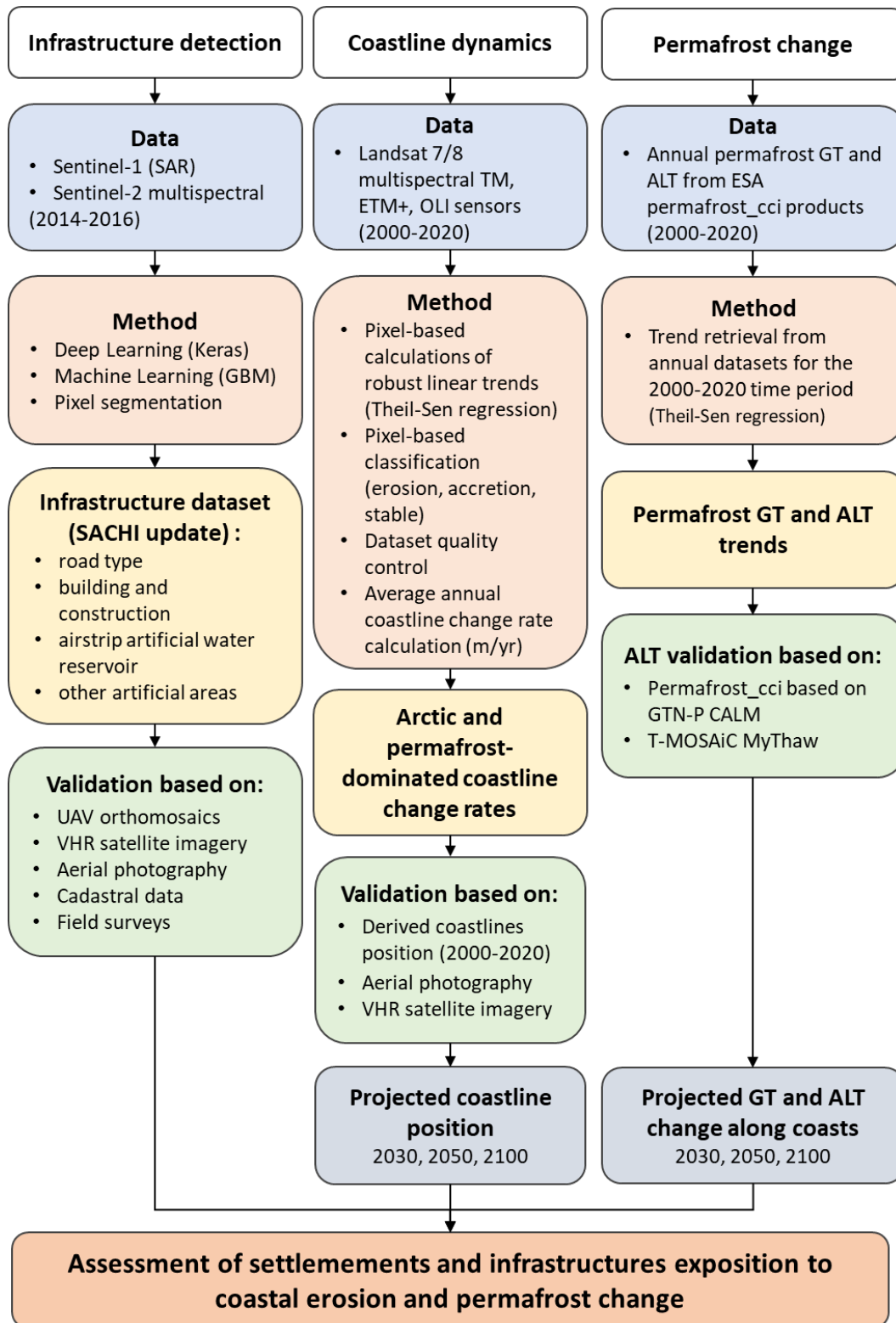


**Figure 3.** Detailed analysis workflow.

## 4.2 SACHI update and validation

The scheme uses Deep Learning (DL; (U-Net convolutional neural network architecture using the deep learning framework Keras) and pixel based Machine Learning (Gradient Boosting machines - GBM) techniques. The DL component uses Sentinel-2 and the GBM component Sentinel-1 and -2. The satellite data and retrieval scheme used in this study is described in Bartsch, Pointner, et al. (2020) and Bartsch et al. (2021). In both cases, DL and GBM, super-resolution processing was applied to the 20 m bands of Sentinel-2 in order to obtain a 10 m nominal resolution dataset for all used bands as input. Atmospheric correction was applied.

The DL component has been extended through the inclusion of additional classes consisting of three road types (asphalt, dirt, undefined) and airstrips/airports. The calibration dataset for all classes has been revised in order to account for inaccuracies in the OpenStreetMap dataset which was used initially. The GBM component also provides a water class by using the pixel based approach. Results for the water class have been separated and added to the database when in proximity to settlements. These water bodies were manually revised and only artificial water bodies (e.g. reservoirs) within settlements kept. This typically includes rectangular or circle-like objects as well as lakes enclosed by open pit mining activities. A k-means post-processing on road features (using the Sentinel-1/2 bands) was applied to evaluate the possibility to distinguish gravel from asphalt roads. The accuracy assessment of the SACHI dataset was done by the computation of confusion matrices and producer, user, and overall accuracy (in %) of the dataset. The producer accuracy represents the percentage objects correctly identified by the modeled dataset. The user accuracy tells the percentage of well predicted objects by the dataset (Llano, 2022). In order to validate object positioning, we compared the new SACHI version to the validation data from UAV orthomosaic, aerial imagery, catastral data and in-situ measurements (Table 1).

## 4.3 Permafrost Coastline Dynamics retrieval and validation

Following the pre-processing method of Nitze et al. (2017), the Landsat time-series were used for pixel calculations of probabilities of erosion and accretion (change from land to water and visa versa) as well as no change, for the time period 2000 to 2020. A threshold for separation of change areas was determined in Bartsch, Ley, et al. (2020). A 50% probability value was found applicable and has been also applied in the present study. The resulting raster information was converted to vector polygons. To facilitate circumpolar implementation several post-processing steps have been introduced. The Landsat results were limited within a 1 km buffer along the coast in order to limit further analyses to coastline related changes, while considering lagoons, deltas and estuaries. Manual quality control was performed to detect and remove mis-classification errors induced by coastal lake change, snow, sea-ice, land-fast ice, tidal changes and infrastructure removal/construction (examples shown in Fig. 4).



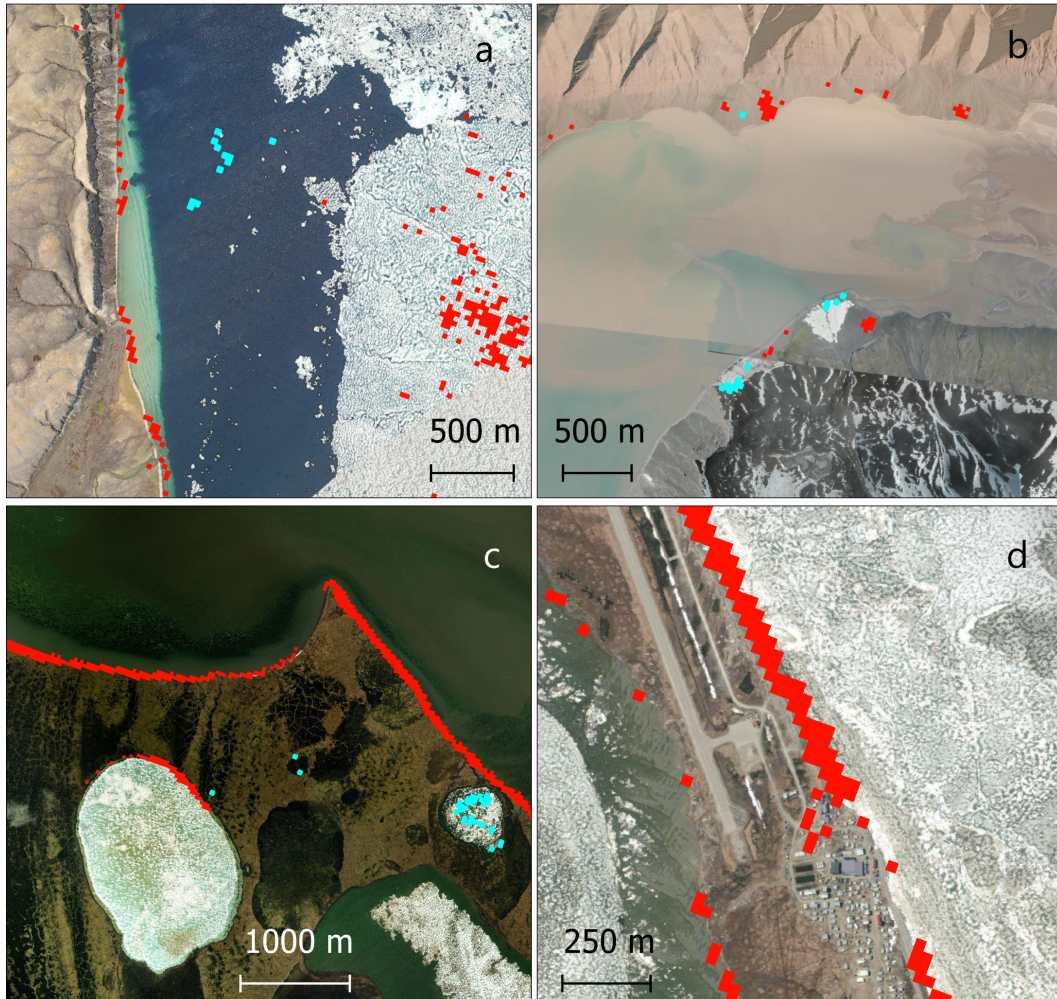


**Figure 4.** Examples of mis-classification errors as seen with the polygons outside of the coastal zone in the raw dataset and needing manual checking and removal. These errors can be induced by sea-ice (a), snow presence (b), lake change (c), or infrastructures (d). The blue polygons show accretion and the red erosion. Background map data sources: Esri©, USGS.

#### 4.3.1 *Coastline change rates retrieval*

A common approach to determine the rate of shoreline change is to use the Digital Shoreline Analysis System (DSAS) developed by USGS which uses time series of vector shoreline positions to calculate rate-of-change statistics at regular spaced perpendicular transects along a coast (Thieler et al., 2009). This method is effective when using manually delineated coastlines, but is not suitable for large automatically extracted datasets. In our case, the nature of the polygonal geometry of the derived change areas allows for a simplified estimation of the average rate of coastline change derived for each polygon. These polygons are in general elongated features, parallel to the coastline. The polygon length and area were calculated. The mean width (average coastline change) was calculated assuming an idealized rectangular representation of the change area. Annual rates of change were subsequently derived. To evaluate the accuracy of this method, we also applied the DSAS workflow to the polygons in test areas by converting the polygons to lines and splitting the shape into a seaward side and a landward side line, corresponding to the 2000 and 2020 coastline in the case of erosion, and vice-versa for accretion. This strategy requires additional manual

editing of the polygons and was also applied to validate the overall quality of the Landsat probabilities, extending the validation of the coastline position in Bartsch, Pointner, et al. (2020) to more sites.

#### 4.3.2 *Coastline position uncertainty*

Calculating the uncertainty linked to coastline positions is necessary in order to evaluate the reliability of the coastline change rates. Equation (1) provides the coastline change rate uncertainty ( $U$ ) which was calculated using the coastline position uncertainty ( $U_{CP}$ ) for each coastline, divided by the number of years of the analysed time period ( $t$ ), (Tanguy, Whalen, Prates, & Vieira, 2023):

$$U = \sqrt{(U_{CP1}^2 + U_{CP2}^2)/(t_2 - t_1)} \quad (1)$$

The coastline position uncertainty is incorporating the image pixel resolution ( $m$ ) and the georeferencing error, RMSE ( $m$ ). The polygons which were retrieved from the Landsat change detection analyses show changes which occurred within a 20-year time-span (2000-2020). The landward and seaward polygon boundaries were defined as the respective coastlines for the year 2000 and 2020. The uncertainty was also calculated for coastline derived from validation data (Table 4).

#### 4.3.3 *Validation of coastline change rates*

Coastline change rates obtained from the Landsat polygons were compared with rates obtained with the DSAS method using validation shorelines. The difference between rates obtained from validation data and from Landsat polygons were calculated for each site, determining the accuracy of the Landsat derived coastline change rates. The End Point Rate (EPR, Thieler et al. (2009)), expressing erosion by negative and accretion by positive values, was used to compare the coastline change rates from the different datasets. In addition, automatic Landsat polygon rates were compared to the DSAS calculated rates for polygons, in order to evaluate the accuracy of this method.

### 4.4 *Permafrost properties evaluation*

For the validation of ALT available from Obu et al. (2021a), we compared the end-of-season ALT (Permafrost\_cci) for a time span of five years from 2015 to 2019 for each of the T-MOSAiC sites (in-situ data, Boike et al. (2021); Martin et al. (2023)). Each grid cell of the Permafrost\_cci dataset contains one ALT value for each year with a spatial resolution of 0.926 km. Buffers of 1 km, 5 km and 10 km radius were implemented around each of the T-MOSAiC sites/transects in which the modeled ALT was combined. Due to the close proximity of the transects at Bayelva and Zackenberg, we defined a single 1 km, 5 km and 10 km radius around these sites.

## 5 *Results*

### 5.1 *Infrastructure mapping*

#### 5.1.1 *SACHI accuracy assessment*

The dataset accuracy was evaluated by comparison with validation data provided from very high resolution data ( $\geq 1$  m), ranging from UAV, satellite and aerial imagery and cadastral data over several settlements (Table 1). The agreement with the 10 m based classification result is 67% with the best detection of 80% for airstrips and other artificial areas such as bare-ground patches, gravel pads, open pit and mining areas (Table 2). Roads show an overall accuracy of 58% and the post-processing results for road types reveal a good

accuracy for the detection of asphalt roads (76%), but only around 40% on average for dirt roads. Buildings are accurately detected in 57% and the minimum building size detectable is 100 m<sup>2</sup>, as determined with the UAVs survey at Paulatuk and Tuktoyaktuk. Figure 5 gives a good visual example of the infrastructure detection detail of the dataset at Tuktoyaktuk. Comparing the dataset with the road survey (in-situ 2021) in Svalbard, reveal the good detection of roads below 10 m width. In fact the dataset was able to detect road widths from 2.7 to 12 m. For the road type survey in Svalbard (asphalt and gravel/dirt) : 75% or the roads samples are detected by the dataset showing mean width of 5.7m. However, only 34% were correctly classified. Among these, 40% asphalt roads were correctly classified with mean width of 6.3 m, and up to 21% regarding gravel/dirt roads showing a mean width 4.9. 28% of the the road width survey samples were not detected.

**Table 2.** Updated SACHI dataset accuracy (10m nominal resolution versus 1m). Producer, User and Overall accuracy values were extracted from computed confusion matrices at each validation site.

| Region           | Validation site | Infrastructures detection accuracy % |         |                 |           |                       |
|------------------|-----------------|--------------------------------------|---------|-----------------|-----------|-----------------------|
|                  |                 | Producer & (User)                    |         |                 |           |                       |
|                  |                 | roads                                |         | others features |           |                       |
|                  |                 | asphalt                              | dirt    | buildings       | airstrip  | other artificial area |
| Alaska           | Atkasuk         | -                                    | 71 (95) | -               | -         | -                     |
|                  | Nuiqsut         | -                                    | 86 (63) | -               | -         | -                     |
|                  | Unalakleet      | 74 (27)                              | 82 (80) | -               | -         | -                     |
|                  | Breving Mission | -                                    | 19 (60) | -               | -         | -                     |
|                  | Chesterfield    | -                                    | 23 (30) | -               | -         | -                     |
|                  | Pruhoe Bay      | 100 (10)                             | 61 (50) | 72 (60)         | 100 (100) | 67 (100)              |
| Russia           | Gasale          | -                                    | 20 (25) | -               | -         | -                     |
|                  | Kathanga        | 100 (5)                              | 24 (75) | -               | -         | -                     |
| West Greenland   | Ilulissat       | -                                    | -       | 42 (60)         | 100 (93)  | 90 (83)               |
|                  | Kangeq          | -                                    | -       | 64 (90)         | 23 (80)   | 64 (90)               |
|                  | Oqaatsut        | -                                    | -       | 30 (30)         | -         | 96 (55)               |
|                  | Qeqertarsuaq    | -                                    | -       | 76 (55)         | 100 (100) | 88 (95)               |
| Svalbard         | Longyearbyen    | 31 (45)                              | 47 (16) | -               | -         | -                     |
| Canadian Arctic  | Tuktoyaktuk     | -                                    | 72 (73) | 50 (79)         | 100 (95)  | 83 (75)               |
|                  | Komakuk         | -                                    | 100     | -               | 84 (100)  | -                     |
|                  | Paulatuk        | -                                    | 40 (33) | 47 (5)          | -         | 72 (60)               |
|                  | Cape Parry      | -                                    | -       | 100 (44)        | 17 (100)  | 70 (81)               |
|                  | Sachs Harbour   | -                                    | 1 (8)   | 6 (12)          | -         | 60 (66)               |
|                  | Ulukhaktok      | -                                    | 49 (80) | -               | 58 (89)   | 71 (86)               |
| Overall accuracy | 67              | 76                                   | 39      | 57              | 80        | 81                    |

### 5.1.2 Updated SACHI dataset

In total, almost 1450 km<sup>2</sup> were mapped in the updated SACHI version, adding 17% more information (Table 3). Artificial water reservoirs were added, accounting for 6902 supplementary features or 138 km<sup>2</sup> and roads have been sub-classified into three different types. Dirt roads represent 50% of the total detected roads and asphalt roads 22%. In total, 408 settlements were attributed to the infrastructures extent within the analysis area, however, only 292 are directly located at the coast. The majority are traditional communities living from fishing, hunting, and herding activity (53%). Industrial settlements for mining activity or gas/oil extraction represent 20% while the remaining settlements represent other uses such as tourism or military, research or weather stations (based on settlement centre data as in Bartsch et al. (2021)). Figure 5 shows a comparison between the first and updated SACHI version, and with validation data at Tuktoyaktuk Peninsula. We note that

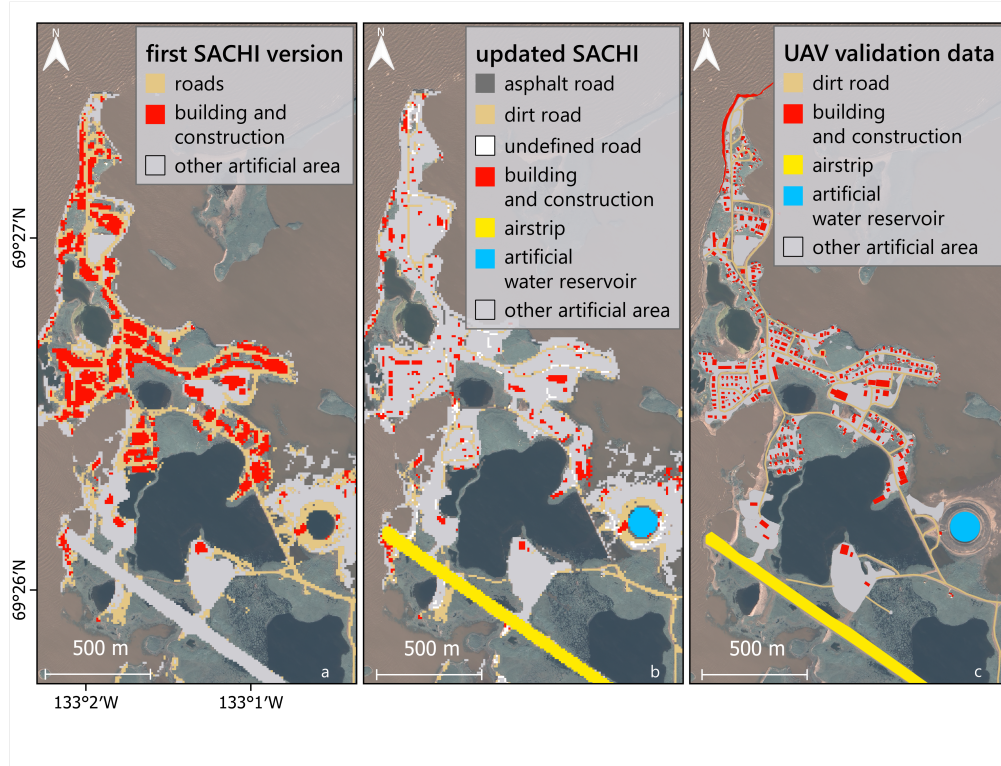


the first version overestimated the extent of areas of buildings and other constructions. The updated version shows significant improvements in the mapping of airstrips, buildings and other constructions with the distinction of individual objects. Artificial water reservoirs are now also included in the dataset.

**Table 3.** Updated SACHI dataset

| Class                             |                             | first SACHI version |                         | updated SACHI version |                         |
|-----------------------------------|-----------------------------|---------------------|-------------------------|-----------------------|-------------------------|
|                                   |                             | n° objects          | area (km <sup>2</sup> ) | n° objects            | area (km <sup>2</sup> ) |
| Roads                             | asphalt                     | 428,872             | 643                     | 293,964               | 123                     |
|                                   | dirt                        |                     |                         | 511,930               | 278                     |
|                                   | undefined                   |                     |                         | 223,701               | 157                     |
| Buildings and other constructions |                             | 219,052             | 199                     | 212,147               | 122                     |
| Other artificial areas            | airstrips                   | 264,732             | 371                     | 2,149                 | 6                       |
|                                   | artificial water reservoirs |                     |                         | 6,902                 | 138                     |
|                                   | other artificial areas      |                     |                         | 225,319               | 625                     |
| Total                             |                             | 912,656             | 1213                    | 1,476,112             | 1449                    |

**Figure 5.** Examples of SACHI versions (a) first (Bartsch et al., 2021), and (b) updated, (c) validation data from the 2019 UAV orthomosaic at Tuktoyaktuk (Canadian Beaufort coast). Background map data sources: Pléiades© CNES, 2018, Airbus DS.



## 5.2 Coastline changes and exposed settlements

### 5.2.1 Coastline changes accuracy assessment

The coastline change rate uncertainty for the Landsat retrieved rates amounts to 2 m/yr (Table 4). The results reveal that on the four validation sites, the coastline change rates between validation and Landsat data can differ from -7.9 to 0.35 m/yr, where positives values represents an overestimation of erosion from the Landsat data and where negatives values represents an underestimation of erosion (Table 5). The comparison between rates calculated with the DSAS extension and the polygon approach shows a very good fit along Barter Island and along the Mackenzie Delta front. Newtok shows a higher difference (-3.4 and -3.7 m/yr) because the retreat has been poorly captured along the mudflat area fronting the settlement, eastward (Fig. 7b). Moreover the validation data was acquired for a shorter time-period than the Landsat data (see Table 1). The Point Lonely site shows the highest difference compared to the validation data, with a large underestimation of the erosion by 7.9 m/yr. This is due to the fact that the Landsat data did not well capture the landward barrier beach migration, as shown in Fig. 6. However, the blufftop retreat was well captured. An additional comparison was made between the Landsat rates using the simplified polygon rate retrieval and the DSAS method. The results show that the automatic method for rate calculation for the Landsat polygons is very accurate and shows an overall underestimation of 0.3 m/yr compared to the DSAS transect based method (last row of Table 5). Regarding these validation sites, we can say that the Landsat polygon rates tends to underestimate the coastline change rates, however, Fig. 6 and 7 show examples of the good fit of the coastline position and calculated change rates of the Landsat derived data.

**Table 4.** Characteristics and errors related to imagery used for validation of the coastline delineation. RMSE stands for "Root Mean Square Error" The RMSE was not considered for the Landsat data since the images are issued from the same source.

| Validation data                          | Acquisition date | Pixel size (m) | Mean RMSE (m) | Coastline position uncertainty (m) | Coverage                     | Coastline change rate uncertainty (m/yr) |
|--|------------------|----------------|---------------|------------------------------------|------------------------------|--|
| Pléiades (multi-spectral, pan-sharpened) | 2018             | 0.5            | 0.35          | 0.6                                | Mackenzie Delta Front        | 0.14                                     |
| Aerial photography (panchromatic)        | 2000             | 1.25           | 2             | 2.4                                |                              |  |
| Maxar WV2 (pan-sharpened)                | 2020             | 0.5            | 1             | 1.1                                | Barter Island                | 0.26                                     |
| Maxar Ikonos (panchromatic)              | 2000             | 0.8            | 5             | 5.1                                |                              |  |
| Pléiades (multi-spectral, pan-sharpened) | 2018             | 0.5            | 0.35          | 0.6                                | Point Lonely                 | 0.28                                     |
| Maxar Ikonos (panchromatic)              | 2000             | 0.8            | 5             | 5.1                                |                              |  |
| Pléiades (multi-spectral, pan-sharpened) | 2019             | 0.5            | 0.35          | 0.6                                | Newtok                       | 0.36                                     |
| Maxar Ikonos (panchromatic)              | 2005             | 0.8            | 5             | 5.1                                |                              |  |
| Landsat-7/8                              | 2020             | 30             | -             | 30                                 | Arctic and permafrost coasts | 2  |
| Landsat-7/8                              | 2000             | 30             | -             | 30                                 |                              |  |

**Table 5.** Inter-comparison between rate calculation methods for validation and Landsat derived data using the DSAS workflow and the polygon geometry method for change rate calculations.

|                      |   | Barter Island | Mackenzie Delta Front | Newtok      | Point Lonely | Air Station |
|----------------------|---|---------------|-----------------------|-------------|--------------|-------------|
| Validation Data      | Represented period                          | 2000-2020     | 2000-2018             | 2005 - 2019 | 2000 - 2018  |             |
|                      | DSAS mean change rate (m/yr)                | -3.01         | -4                    | -12.9       | -15.8        |             |
|                      | Uncertainty (m/yr)                          | +/- 0.26      | +/- 0.14              | +/- 0.36    | +/- 0.28     |             |
| Landsat derived data | Polygons mean change rate (m/yr)            | -3.36         | -3.54                 | -9.2        | -7.9         |             |
|                      | DSAS mean change rate (m/yr)                | -3.63         | -4.1                  | -9.5        | -8.02        |             |
|                      | Uncertainty (m/yr)                          | +/- 2         | +/- 2                 | +/- 2       | +/- 2        |             |
| Difference           | Validation - Landsat Polygon rates (m/yr)   | 0.35          | -0.46                 | -3.7        | -7.9         |             |
|                      | Validation - Landsat DSAS rates (m/yr)      | 0.62          | 0.1                   | -3.4        | -7.78        |             |
|                      | Landsat Polygon - Landsat DSAS rates (m/yr) | 0.27          | 0.56                  | 0.3         | 0.12         |             |

### 5.2.2 Settlements exposed to coastal erosion

Over the time period 2000-2020, significant coastline position changes were detected along 292 settlements located directly at the coast. These changes represent a total of 476 km of coastline length showing an average change rate of -0.8 m/yr, where erosion is dominating 70% of the investigated coast. Accretion is located along mobile coastal forms such as barriers islands, beaches and spits (Table 6). Settlements and infrastructures potentially affected by coastal erosion by 2030, 2050 and 2100 were identified based on a linear extrapolation of erosion rates, based on the 2000-2020 time-period (Appendix A2)

According to this extrapolation, 16% of the coastal settlements will be subject to infrastructure damage or loss due to coastline retreat in 2030 and up to 23% in 2100. Along these specific settlements, the average erosion rate is about -3.2 m/yr. The difference in the amount of affected settlements arises from the fact, that some settlements are built a bit more inland and will only get affected later. By 2100 the total surface area of infrastructures (as detected with the 10 m resolution ) potentially at risk from by coastal erosion equals to 17.8 km<sup>2</sup>, including bare-ground areas (see Appendix A1). The Alaskan coast stands out, with 25 settlements exposed to coastal erosion by 2100, showing average erosion of 3.6 m/yr. In Russia, the majority of exposed settlements is located along the Chukchi Peninsula (12), and Central Siberia coast (20, Laptev and Kara Sea). In Svalbard, Longyearbyen, Barentsburg, and Svea are suspected to be affected by coastal erosion by 2100. In Canada, the settlements of Tuktoyaktuk, Stokes Point and Kugluktuk were identified at risk. In Greenland, no settlements were estimated at risk from coastal erosion. Note that the majority of the Greenland coastline consists of solid rock and erosion is limited to unconsolidated cliffs (Luetzenburg et al., 2023). Due to ice recent ice loss, deltas shows a prograding trend in Greenland (Bendixen et al., 2017). Moreover some areas are experiencing glacial isostatic rebound. Coastline change rates below 2 m/yr were not considered in the study due to their non-significance defined by the Landsat coastline change rate uncertainty (U).

**Table 6.** Coastline dynamics at settlement vicinity for the period 2000-2020

|                                    | n° of settlements | mean change rate<br>(m/yr) | erosion             |                     |                | accretion           |                     |                |
|------------------------------------|-------------------|----------------------------|---------------------|---------------------|----------------|---------------------|---------------------|----------------|
|                                    |                   |                            | mean rate<br>(m/yr) | max. rate<br>(m/yr) | length<br>(km) | mean rate<br>(m/yr) | max. rate<br>(m/yr) | length<br>(km) |
| <b>Total coastal settlements</b>   | 292               | -0.8                       | -2.9                | -20.4               | 336            | 3.2                 | 12.7                | 140            |
| <b>Exposed settlements in 2100</b> | 69                | -1.8                       | -3.2                | -20.4               | 150            | 2.9                 | 4.5                 | 20             |

Very high erosion rates up to 19 m/yr are found along the Alaskan Beaufort coast at Point Lonely Air Station (190 km eastward of Prudhoe Bay; Fig. 6). The back-shore of this area is characterized by tundra dissected by ice-wedge polygons, where erosion is characterised by block failure along the bluff. To the east, the coastline is characterized by an enclosed lagoon of 2 km length and 0.7 km width which is facing the airstrip. As a continuation of the fast erosion of the tundra cliffs, the lagoon's barrier beach was also moving very rapidly towards the mainland in the last 20 years. A major coastline retreat phase occurred during the last decade, after 2009, as seen on Figure 6. The retrieved data from Landsat trends show that the bluff-top retreat has been well captured in this area. However, we note a clear rupture in the retrieved change area at the level of the barrier beach enclosing a coastal lagoon, where its retreat has not been well captured (Fig. 6). These specific coastal land-forms are prone to rapid changes during storm events, potentially impacting their width. It is possible that the barrier beach became so narrow during its retreat phase, that it was not detected in the Landsat data, so that it was not possible to distinguish between the coastal lagoon and open ocean. Moreover, the turbidity of the lagoon waters could have influenced the Landsat pixel classification.

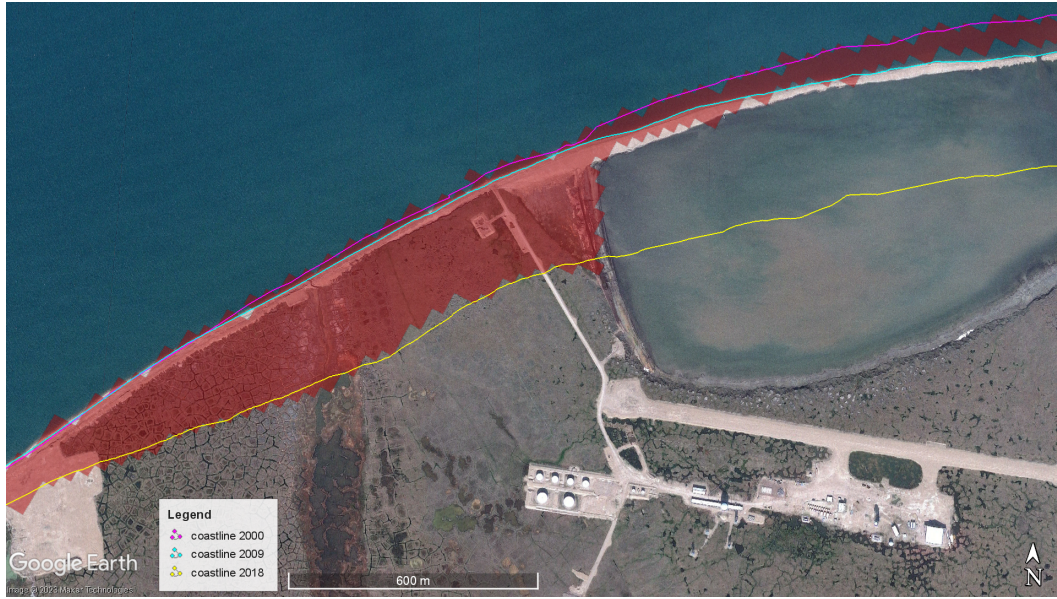


**Figure 6.** High erosion and infrastructure loss at Point Lonely Air Station. The imagery is from July 2009. The red overlapping area represents erosion area retrieved from Landsat trends. We note a very good fit with the shorelines of 2000 and 2018 along the bluff, however the barrier beach migration was not well captured. The coastlines positions were derived from VHR satellite imagery corresponding to Ikonos©-2000 (0.8 m spatial resolution); WorldView-1-2009 (0.5 m) and Pléiades© CNES/Airbus-2018 (0.5 m). Background map data source: Google, ©2009 Maxar Technologies.

Considering linear erosion rates, we estimate that infrastructure of a total of 45 settlements will get affected by coastal erosion by 2030 and 69 settlements by 2100. These settlements are mainly associated with residential areas with traditional food-harvesting activities (45%) and 33% with gas/oil and mining industry. Other affected settlements are abandoned or are military or weather stations. Coastline change rates estimated at Barter Island show a good fit with validation data and reveal significant retreat averaging 3.4 m/yr in front of the bluff-top (visible as red overlapping areas in Fig. 7a). Some accretion area is present along the barrier island and spits (northwest) and a beach (600 m length) at the northeast sector of the island. It seems to grow at a rate of 4.2 m/yr. The coastline position estimated in 2100 shows a potential loss of infrastructures due to coastal erosion such as the front road of the island and a part of the radar station of Kaktovik (Fig. 7a). Along the Bering sea, the traditional settlement of Newtok (Fig. 7b) is also a good example of high erosion rates, which will cause a loss of the majority of the infrastructures if no relocation plan is implemented. This is evident in the projected coastline positions for the mid- and long-term (Fig. 7b). The projected coastline positions may underestimate areas at risk (from the airstrip towards the east) as seen with the difference between the red overlapping area and the validation coastlines. Although our projections are conservative, they do show the loss of infrastructure over the mid- and long term periods.



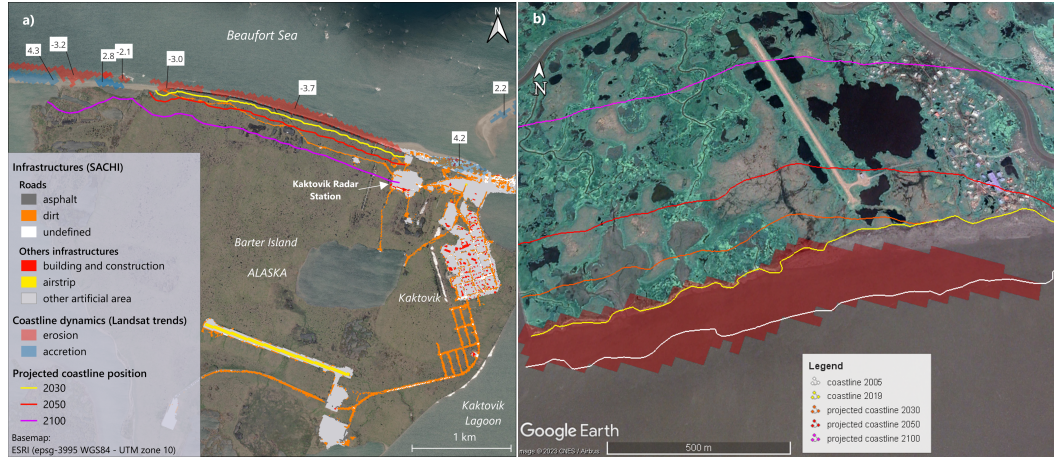


**Figure 7.** Example of results with merged infrastructure and coastline dynamics datasets, showing potential loss of infrastructures at a) Kaktovik (U.S. Beaufort Sea) and at b) Newtok (U.S. Bering Sea). At Barter Island (a), the front road and the radar station may be affected in the long-term. At Newtok, averaging 9.2 m/yr, coastal erosion has already destroyed infrastructures. In case erosion continues at such a great pace, the majority of the settlement is expected disappear by 2100 (purple line). The coastline positions were derived from VHR satellite imagery corresponding to Ikonos©-2005 (0.8 m spatial resolution) and Pléiades© CNES/Airbus-2019 (0.5 m). Maps Data: a) ESRI; b) Google, ©2019 CNES / Airbus.

### 5.3 Warming permafrost and exposed settlements

#### 5.3.1 Active Layer Thickness validation

The comparison between the T-MOSAiC 2021 myThaw dataset (Martin et al., 2023) and the Permafrost\_cci ALT is displayed in Appendix A5. Due to the lack of Permafrost\_cci model results for 2020 and 2021 we compared different time periods (Permafrost\_cci end-of-season ALT: 2015 to 2019, T-MOSAiC: all ALT measurements from 2021). The Permafrost\_cci ALT and the measured ALT data agreed well for the following stations: Samoylov (Siberia, Russia; A5c). Toolik Lake (Alaska, USA; A5d) and the Zackenberg "wet" transect (Greenland; A5g). Differences between the modeled and measured data can be explained with the nature of the T-MOSAiC measurements which are obtained throughout the whole summer whereas the Permafrost\_cci ALT is the end-of-season value. Hence, the seasonal evolution of the ALT is not captured by the modeled dataset. We found major disagreements for the following sites: (both) Bayelva transects (Svalbard, Norway; A5a), Kevo Vaisejaeggi (Finland; A5b), Siksik Creek (Trail Valley Creek, Canada; A5e), Cambridge Bay (Canada; A5f) and the Zackenberg "dry" transect (Greenland; A5g).

The two T-MOSAiC sites in Svalbard showed a high spatial variability despite their proximity (about 500 m). The median ALT (1.2 m and 0.8 m respectively) was best represented within the Permafrost\_cci ALT dataset in the 10 km radius around the T-MOSAiC sites as the outliers of the box-plot are in range of the measured ALT (A5a). Both sites were located within one grid cell. This outlined one of the challenges as the different site specifics (i.e. soil properties, snow cover, vegetation height, water level) led to very different ALT which are not reproduced by the model as the spatial resolution is too coarse (0.926 km). The same issue applies to the Zackenberg transects as the T-MOSAiC ALT measured at the "dry" transect extended the ALT measured at the "wet" transect and the Permafrost\_cci ALT shown in A5g). For the T-MOSAiC sites Kevo Vaisejaeggi and Siksik Creek, the Permafrost\_cci ALT was at least twice as high as the measured values (A5b,e).



It was vice versa for the T-MOSAiC sites at Cambridge Bay (A5f) where the measured ALT is almost three times the modeled ALT.

A comparison between the T-MOSAiC, CALM and Permafrost\_cci ALT (10 km radius) sites is illustrated in Appendix A6a-g. In Svalbard (A6a), we found a larger difference between the median ALT for the Permafrost\_CCI ALT and the CALM than for the other study sites. The median Permafrost\_cci ALT was 0.31 m compared to 1.56 m for the CALM site within 60 km radius and 1.01 m and 0.95 m for the sites located within 120 km. In Kevo, Finland, (A6b), the Permafrost\_cci ALT showed higher variability than the T-MOSAiC and CALM sites. The T-MOSAiC sites generally showed lower thaw depths than both Permafrost\_cci ALT and the CALM sites in Kevo and in Siksik Creek (A6b,d). In Samoylov (A6c), the Permafrost\_cci ALT and CALM site within 60 km showed the same median thaw depth (0.51 m) whereas the thaw depths at the T-MOSAiC site (median 0.36 m) was more similar to the CALM sites at a radius of 120 km (median thaw depths 0.35 m and 0.41 m). The T-MOSAiC dataset from Toolik lake in Alaska (A6e) showed higher variability than both the Permafrost\_CCI ALT and CALM datasets and the median thaw depths for the T-MOSAiC dataset agreed better with all the CALM sites compared to the Permafrost\_CCI ALT dataset. Since no CALM site was located within 400 km of the T-MOSAiC site in Cambridge Bay (A6f), only the comparison to the Permafrost\_CCI ALT is shown. The median thaw depth of the T-MOSAiC dataset at this site was 0.52 m higher compared to the thaw depth of the Permafrost\_cci ALT dataset. In Zackenberg, the T-MOSAiC “dry” dataset was more similar to the CALM dataset whereas the “wet” T-MOSAiC dataset was more similar to the Permafrost\_cci ALT dataset.

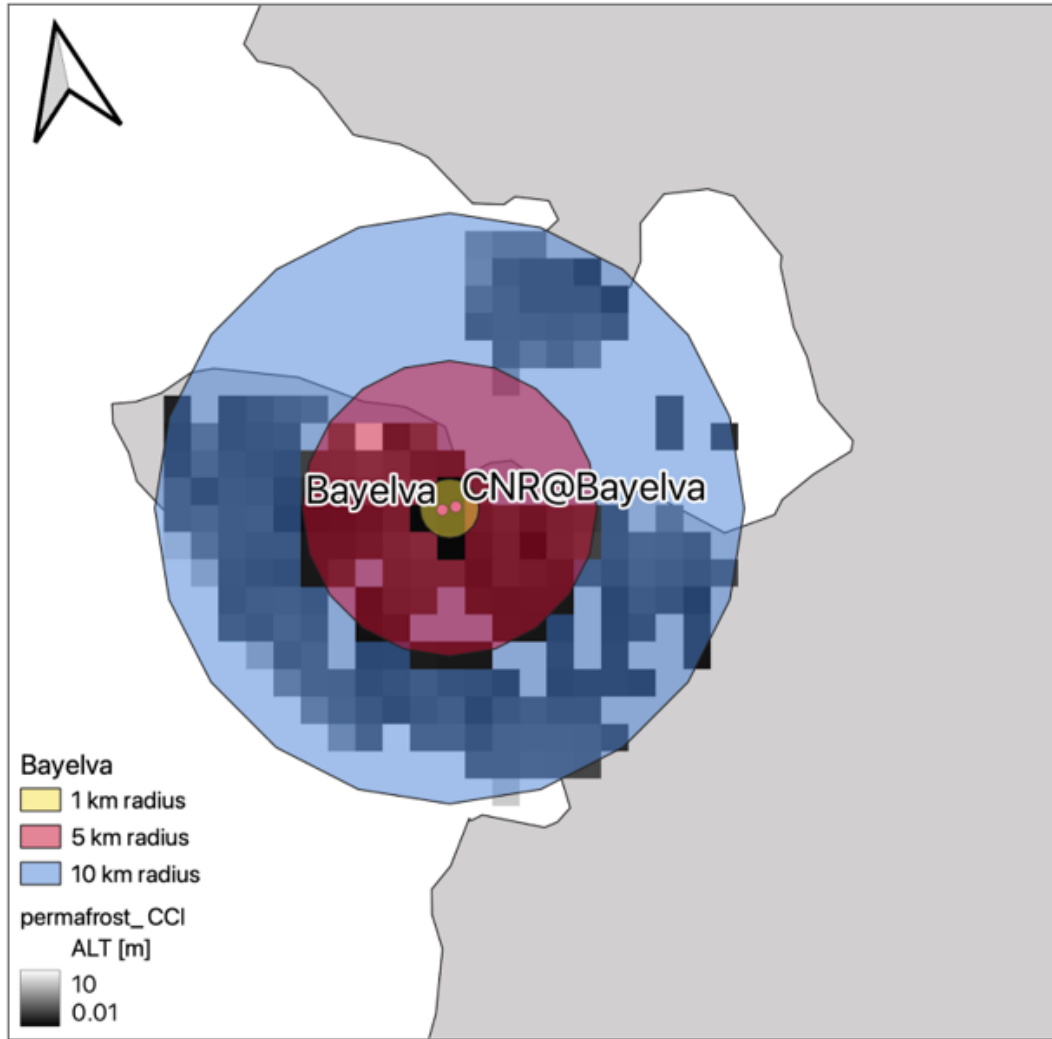


**Figure 8.** The 1 km (yellow), 5 km (red) and 10 km (blue) radius for the T-MOSAiC site Bayelva which were defined to crop the Permafrost\_cci ALT data sets from 2015 to 2019. The (grayscale) color bar for the Permafrost\_cci ALT is from 0.01 to 10 m.

### 5.3.2 Projection of permafrost conditions and exposed settlements

The results of the Permafrost\_cci time-series shows that since the last 20 years, the GT of northern permafrost dominated coasts is warming at a global average rate of  $+0.10^{\circ}\text{C}/\text{yr}$  (Fig. 8a (white box) with maximum values up to  $+0.25^{\circ}\text{C}/\text{yr}$ ). We note a high variability between coastal regions, with Svalbard and Siberian coasts showing GT trends above global average. The Central Siberian coast shows the highest average GT change of  $+0.16^{\circ}\text{C}/\text{yr}$ , however, the highest rates (above  $0.20^{\circ}\text{C}/\text{yr}$ ) are found for the Canadian Arctic, Greenland, Svalbard and Western Siberian coasts.

Looking at the ALT, the model shows less variability (Fig. 8b). The global average change rate is about  $+0.01 \text{ m}/\text{yr}$  (white box), with maximum rates up to  $+0.09 \text{ m}/\text{yr}$  (Hudson Bay area). The highest average ALT rate is found along the European Plain coast ( $0.03 \text{ m}/\text{yr}$ ). Note that the model also represents decreasing GT for the Canadian Arctic and Greenland coasts with minimum values down to and  $-0.15^{\circ}\text{C}/\text{yr}$ . The ALT shows minimum

values from -0.04 to -0.07 m/yr along the coasts of Alaska, Hudson Bay, Greenland and Western Siberia.

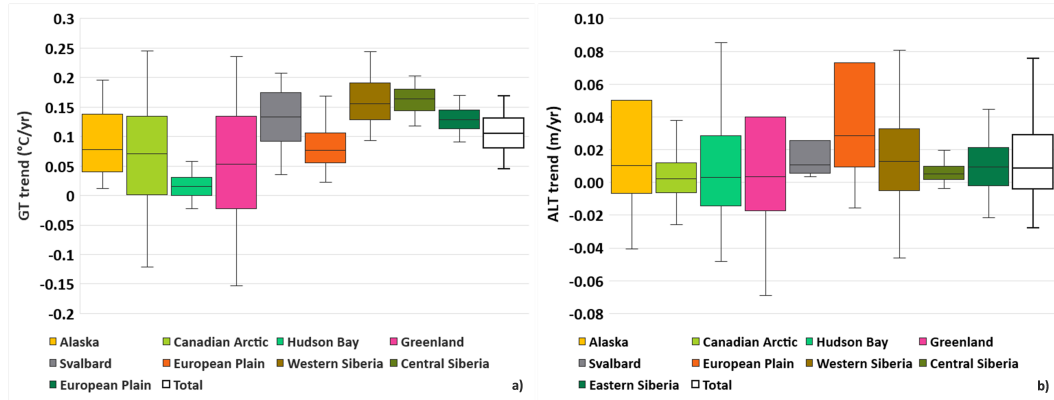


**Figure 9.** Annual trends for ground temperatures (at 2 meters depth) and active layer thickness per regions. The extent considered corresponds to the SACHI limits (100 km coastal zone). The trends were calculated over the 2000-2020 period using the datasets of Obu et al. (2021b) and Obu et al. (2021a).

By 2100, the average coastal permafrost GT is expected to increase by 8°C and the ALT by 0.9 m. The trend projections for 2100 suggest extreme GT warming above 9°C all along the Russian coast as well as along the Beaufort Sea coast, the mouth of the Amundsen Gulf and Eastern Greenland (Appendix A4, A3).

Among the total infrastructures mapped, 65% are located on ground estimated to warm between 5 to 15°C by 2100, representing 65% of the settlements, and 35 % of the identified exposed settlement area are expected to experience ALT increase between 1 to 5 m by 2100.

For the settlements identified to be exposed to infrastructure damage from coastal erosion by 2100, the ALT is expected to increase by an average of 1.5 m and GT by 9.7°C by 2100. The majority (60%) of settlements are located on ground temperature increase at 2 m depth ranging from 4 to 12°C and ALT increase from 0.5 to 2 m/yr (Fig. 9). The highest GT increase (+17.8°C) was estimated at the settlement of Valkumey (East Siberian Sea) and the highest ALT increase (+6.14 m) at Shaktoolik city (Bering strait). In 2019, the ALT was estimated at 0.9 m for at exposed settlements. The highest ALT was found at an Alaskan exposed settlement in 2019 (1.8 m) and could potentially reach up to 2.3 m in 2100. Settlements in Canada, Svalbard and Russia show ALT less than 1 m depth in 2019. ALT is expected to more than double by the end of the century. Canada shows the lowest average ALT in 2019, due to the northern location of exposed settlements (Fig. 10)

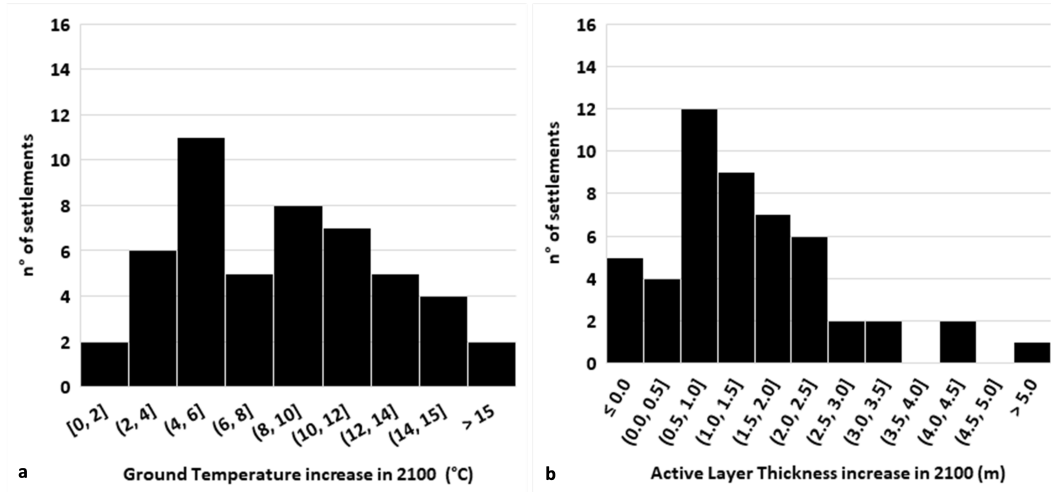


**Figure 10.** Associated ground temperature and active layer thickness change at identified settlements at risk from coastal erosion by 2100.

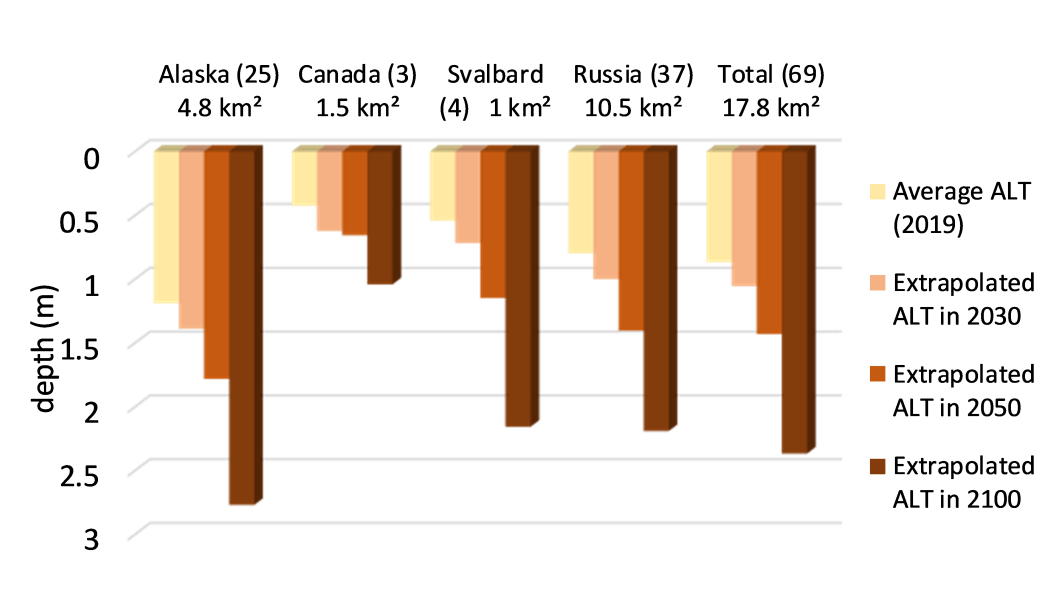


**Figure 11.** Active Layer Thickness (ALT) and extrapolation for different time-periods. ALT was estimated at infrastructure extent of settlements at risk from coastal erosion and averaged per region.

## 6 Discussion

### 6.1 Infrastructure identification

In this study, our focus was on analyses of settlements and infrastructure occurring along permafrost-dominated coastal areas. The new SACHI dataset provides improved information on infrastructure occurrence in the Arctic, particularly for roads, airstrips and artificial areas. Due to the limitation to 10 m nominal resolution, 33% of individual human

related features were not captured across the validation sites. Specifically road and building detection is challenging. The amount of detectable buildings is controlled by the resolution and the quality of the Sentinel-2 data (multi-spectral), which limits the detection of small constructions, and object mis-classification can occur with the presence of snow patches, rock outcrops, landfills, construction debris and large driftwood accumulations along the shore. Asphalt roads are scarcely present in the Arctic and along permafrost coasts, since the majority of roads are made of dirt or gravel which is easier and cheaper to construct and maintain. In some settlements, roads are made of concrete blocks, falling in the undefined category. Although the Sentinel-2 imagery has been processed for atmospheric corrections (aerosol optical thickness and water vapour), clouds are still influencing the data quality and can lead to mis-classification in addition to calibration and training data issues. The DL and GBM algorithms were trained on specific areas, however, the heterogeneity of geographic regions across the Arctic and along permafrost coasts may influence the performance of the algorithms. It could be shown that Sentinel-2 allows to capture also roads below 10 m width in some cases. Individual building detection needs to be improved with DL and GBM using VHR optical images. However their processing remains challenging at regional scale. The Sentinel-1 SAR images were used for the GBM processing. Distortion, noise, and incidence angle inherent to SAR images may affect image quality and result in detection issues of spatial features (Kumar, 2021). Moreover, air and ground temperatures are critical parameters influencing back-scatter values (Bergstedt et al., 2018). However, the assessment shows that the 10 m spatial resolution allows consistently identifying human impacted areas such as very small settlements with few houses, which need to be considered in risk assessment studies across the entire Arctic. However, our results remains conservative in the estimation of potential risks on communities and infrastructures.

## 6.2 Coastline changes

The use of consistent Landsat time-series for the detection of coastline changes within 20 years shows to be efficient to provide estimations of average coastline rates on a regional to pan-Arctic scale. Although the results agree with validation data, it is important to note that coastline changes below 2 m/yr were not considered in the analysis since they were below the detection threshold. This results in an underestimation of coastal changes, since the majority of permafrost-dominated coast is estimated to erode at a pace of up to two meters per year and areas of accretion are comparatively scarce (B. Jones et al., 2020; Irrgang et al., 2022). According to the results, the prevailing mechanism of coastline changes in the vicinity of settlements is erosion. Accumulation was detected relatively rarely. Moreover, local and regional studies based on the analysis of VHR imagery, coastline erosion has been accelerating in recent years in various areas of the Arctic (Tanguy, Whalen, Prates, & Vieira, 2023; Whalen et al., 2022) revealing potential economic risks (Ogorodov et al., 2020). The assessment of coastline changes at the regional scale, as well as the detection of inter-annual variability of coastline changes remains a challenge when using open-access satellite data. Compared to transect-based analyses (DSAS), our study estimates only average rates within changing areas, and does not consider regular transects spacing such as in the DSAS framework. Moreover a shoreline reference is not consistently defined with this method. In fact, the Landsat trends detect change from water to land and land to water and do not consistently allow to distinguish between the retreat of a bluff-top or a waterline and visual checking is necessary to evaluate if erosion is associated to bluff-top retreat such as along the Beaufort coast, or due to sediment migration as along barrier islands and spits. Tanguy, Whalen, Prates, and Vieira (2023) have shown differences in coastline change rates measurement up to 20% when considering blufftop/vegetation line or waterline between as a shoreline reference. For the purposes of coastal risk assessment along permafrost coasts with the projection of future coastline position, it is necessary to characterize retreat of the bluff-top line rather than migration of mobile deposition sedimentary features such as beaches, spits and barrier islands. Note that other factors, such as sea level rise, depression flooding or thermokarst lake breaching can induce future rapid and extensive coastline retreat and

were not considered in the present study for the projected coastline position. The projected coastline position does not consider potential erosion acceleration or flooded areas which can significantly influence inland water progression.

### 6.3 Permafrost thaw

The GT and ALT Permafrost\_CCI products have been validated with various in-situ measurements. However, the datasets reveal regional biases associated with the spatial resolution (near 1 km) of the modeled datasets which do not capture land-cover spatial variability at a finer scale. Ground stratigraphy and snow cover are significant controlling factors for ALT. The currently used ground stratigraphies in the Permafrost\_cci modelling are derived from land-cover classification (Westermann et al., 2015; Palmtag et al., 2022) and do not consistently represent real ground conditions. Hence, significant errors are expected where bedrock is actually represented as moisture-rich ground. Thus, the characterization of change using relative values is more adapted than the use of absolute values. However, note that this study is not considering actual ALT and that its increase may not be always synonym of increasing vulnerability and subsidence risk. Since the study area extends over the arctic region and considers permafrost dominated coasts, some areas may show deep active layer thickness where its increasing trend is less relevant for risk assessment. Increasing ALT might be relevant in areas characterized by shallow ALT, such as higher latitudes Arctic settlements where subsidence and infrastructure instabilities can be caused by abrupt thaw depth. Permafrost temperature trends can be also used as a proxy to assess areas with risk of thaw subsidence. The experimental study by Wagner et al. (2018) has shown the significant effect of increasing GT with permafrost thaw, by the deepening of the permafrost table and subsidence. Based on an area of 143 m<sup>2</sup>, and 1.5 m soil depth, their results reveal a linear relationship between GT increase and subsidence where an augmentation of 13 °C results in ALT increase of 1 m and subsidence of 10 cm. Projections for GT reveal that 27% of the studied area (100 km coastal fringe) will potentially face changing GT of above 10 °C by 2100, coinciding with 34% of the total mapped infrastructures area, which could potentially be affected by subsidence and infrastructure damage.

Studies have shown that summer surface deformation is derivable over low-land permafrost regions from Sentinel-1 SAR. In the area of Point Lonely Air Station ground surface displacement ranged between 2-6 cm in the summer 2017. However, long time series and in-situ data are lacking to confirm the recorded subsidence within the InSAR pixel scale (Strozzi et al., 2018). Assessment of risk areas associated to increasing ALT would need to consider the actual ALT. Moreover, increase of GT and ALT may lead to enhanced thermokarst process, with the alteration of permafrost land-forms that could significantly affect the Arctic hydrology (Grosse et al., 2013; Liljedahl et al., 2016; Tanguy, Whalen, Prates, Pina, et al., 2023). Furthermore, permafrost thaw alters Arctic hydrology (Grosse et al., 2013; Liljedahl et al., 2016; Tanguy, Whalen, Prates, Pina, et al., 2023) and enhances thermo-hydrological erosion, which may lead to dispersion of contaminants from toxic leakage of buried wastes and landfill at industrial sites (Langer et al., 2023).

### 6.4 Exposed infrastructures and settlements to coastal erosion

The combined analysis of the coastline change dataset and the updated SACHI dataset allows the identification of settlements at risk from coastal erosion, from short- to long-term periods (2030, 2050, 2100). In some locations, the results are coherent with local measurements, such as the study of Nicu et al. (2021), which investigated coastline changes and potential impacts on the cultural heritage site of Hiorthhamn in Svalbard (78°14'50" N, 15°42'30" E). Our pan-Arctic approach was able to identify 52 coastal settlements in Alaska (within study area extent), with 25 settlements being exposed to coastal erosion by 2100. The results agree for 11 settlements, also identified by the study of Buzard et al. (2021) with identification of 14 additional settlements mostly located along the Beaufort Sea coast. However, note that the magnitude of coastline change considered can affect the

detection of exposed settlements. Note that some communities are also affected by river migration hazards which are important in delta regions. Moreover, the present study does not consider future external factors which may increase or reduce erosion rates (sea level rise, subsidence, beach accretion). Hence, our approach does not replace local detailed analyses which remains necessary at individual settlements, for the identification of coastal risks.

For the first time, our dataset allows for a pan-Arctic estimation of the amount of settlements being exposed to oncoming and future coastal erosion, warming permafrost temperatures and active layer thickening. However, the very likely intensification of drivers of coastal erosion, such as storm surges and lengthening of the open water season, were not incorporated in our analyses. Thus, it is likely that our results present a rather conservative estimation of the total number of coastal settlements being affected by coastal erosion in the future. The assessment of infrastructure damage and associated costs within coastal areas needs to be assessed in order to quantify economic consequences (D. A. Streletskiy et al., 2019b; Buzard et al., 2021; Ogorodov et al., 2023).

## 7 Conclusions

Our study has demonstrated the effectiveness of remote sensing techniques in assessing the evolution of arctic and permafrost coastlines over the last 20 years. The results show that erosion dominates along coastal settlement areas (70%), with retreat rates of up to 19 m/yr. Extrapolation of the coastline position for 2100 reveals that 23% of coastal settlements will be affected by coastal erosion, with a total estimated infrastructure loss/damage area of 18 km<sup>2</sup>. The majority of identified exposed settlements are localized along Alaskan and Siberian coasts. Simultaneously, ground temperature has shown a significant warming trend, and the active layer is thickening. By 2100, it is estimated that ground temperatures of the permafrost coastal zone will have risen by 8°C and the active layer by 0.9 m. These changes in ground conditions are subject to enhanced permafrost degradation, damaging infrastructure and populations' livelihoods. Indeed, 65% of infrastructures are built in areas where ground temperatures are expected to rise between 5 and 15°C, and 35% over active layer thickness increase between 1 to 5 meters. These trends indicate a potential increase in ground subsidence, flooding hazards and changes in hydrological systems. To minimize the risks and costs faced by coastal permafrost communities, coastline management and adaptation strategies need to be adopted rapidly.

In a context of changing permafrost conditions, this work provides relevant information at the pan-Arctic scale for the identification of settlements and infrastructures at risk by the end of the century. This is an important first step towards developing mitigation strategies and thus reducing the vulnerability of Arctic settlements to future coastal hazards.



**Appendix A Additional maps, figure and tables.**

**Figure A1.** Rapid coastal erosion threatening coastal infrastructures at Utqiagvik (Barrow, Alaska) after a storm during the summer 2023. A road portion was destroyed and we note the presence of a red tank and remaining big-bags down the bluff. Blufftop failure is occurring as seen on inset (b). Image credit: Ben Jones



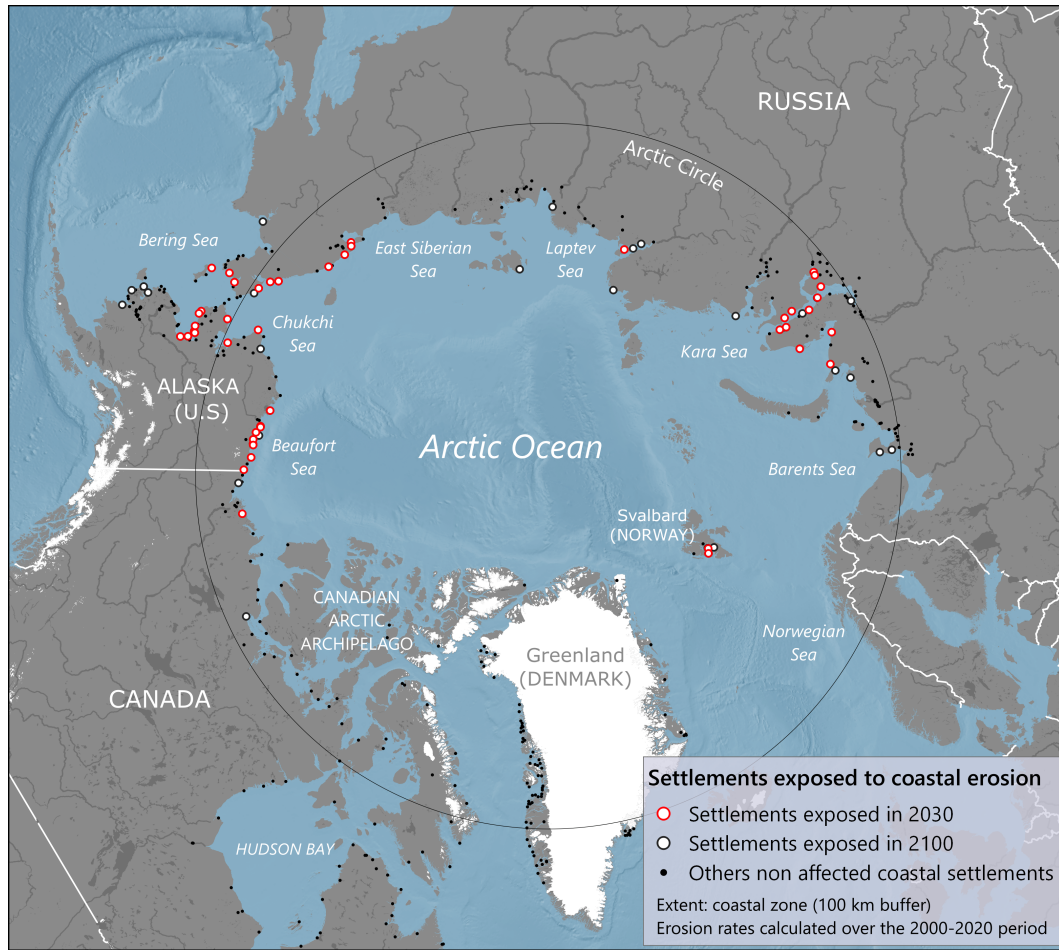


**Figure A2.** Settlements potentially exposed to coastal erosion. Contains modified Copernicus Sentinel data 2016 to 2022.

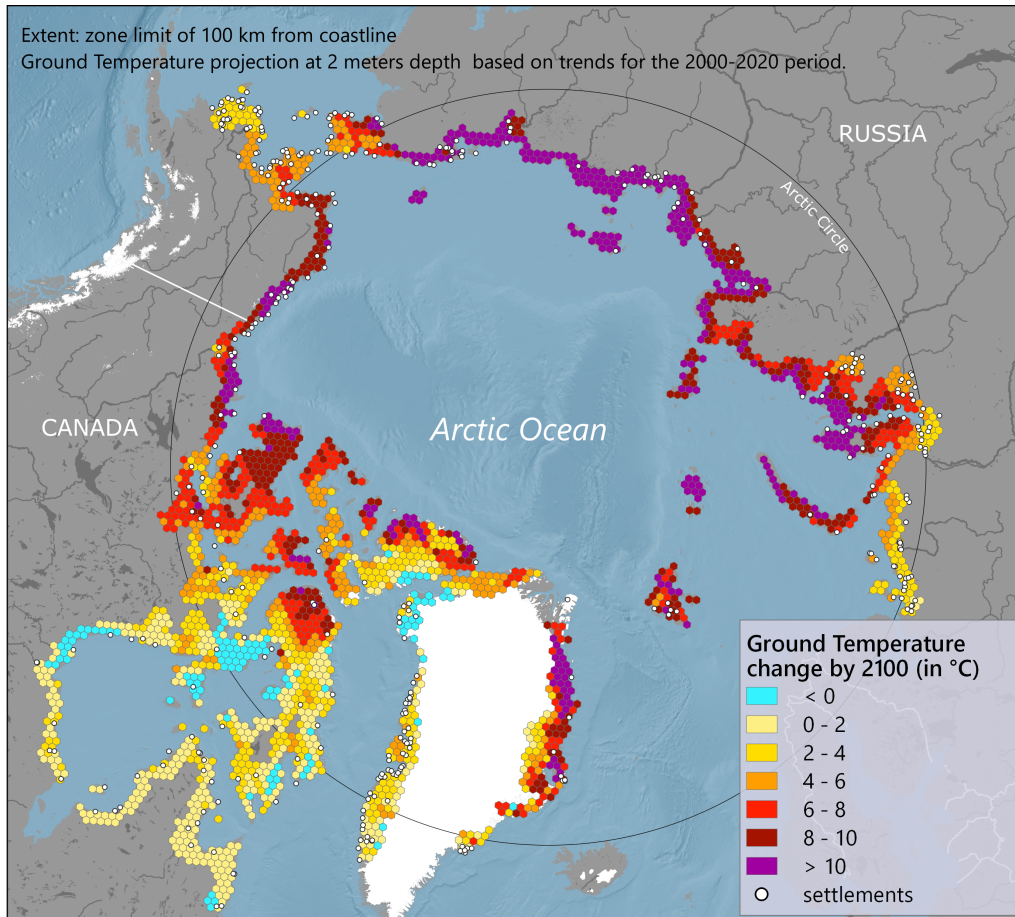


**Figure A3.** Ground temperature change in by 2100 based in trends derived from Permafrost\_cci data (Obu et al., 2021b). The hexagons are width and height is 50 km and the ground temperatures trend for the period 1999-2020 were averaged within the hexagons.

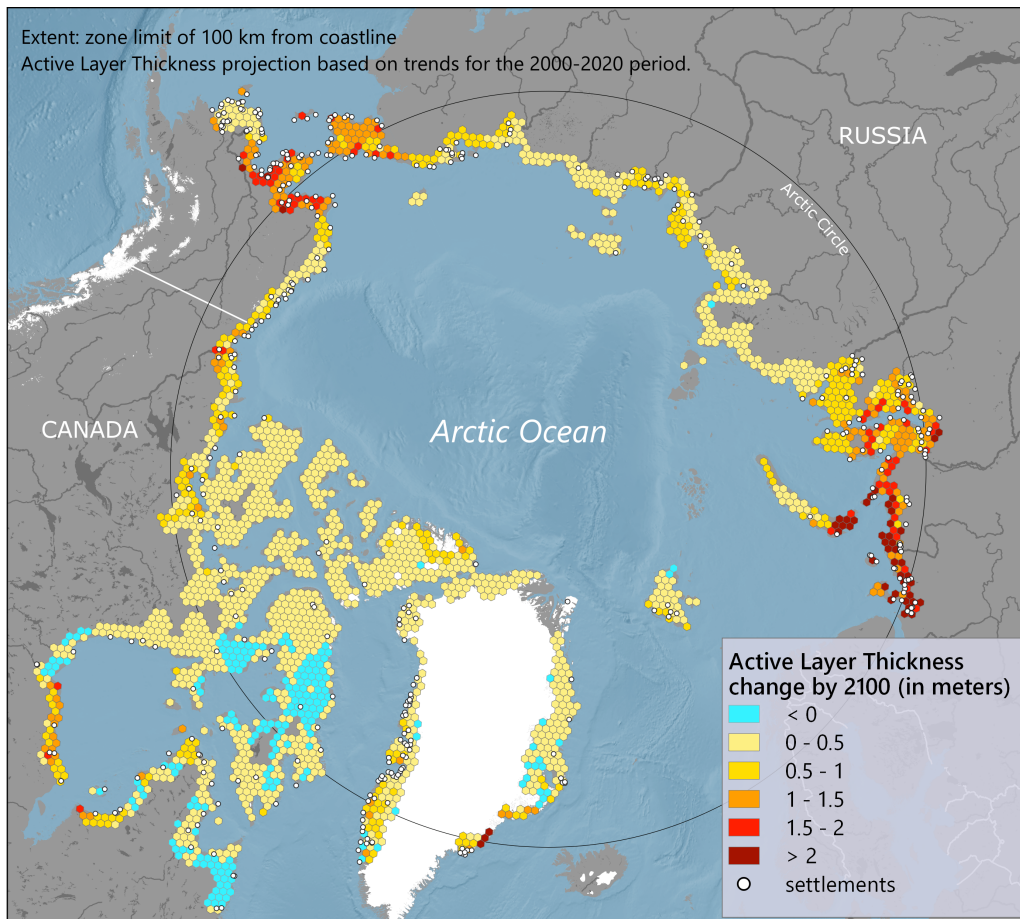


**Figure A4.** Active Layer Thickness change by 2100, within the 100 km zone from the coast.

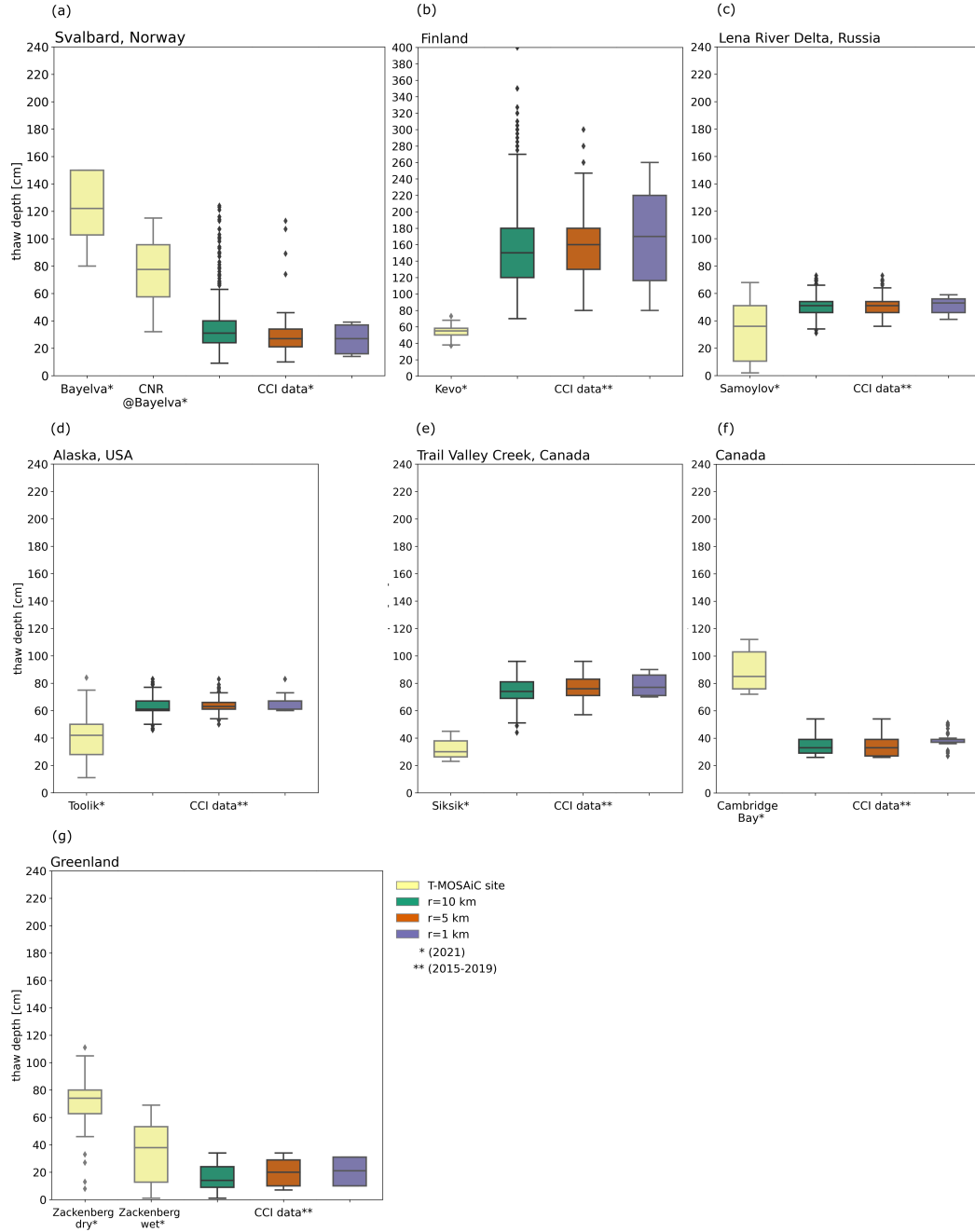


**Figure A5.** Comparison of the T-MOSAiC 2021 myThaw dataset with the output from the ESA Permafrost Climate Change Initiative (Obu et al., 2021a) end-of season ALT product from 2015 to 2019 for all eight sites. The Permafrost.CCI ALT output was read out for a 1 km, 5 km and 10 km radius around each of the eight T-MOSAiC stations, except for the two Bayelva sites (a) and the two Zackenberg transects (g) where one model ALT output was generated due to close proximity of the site locations.

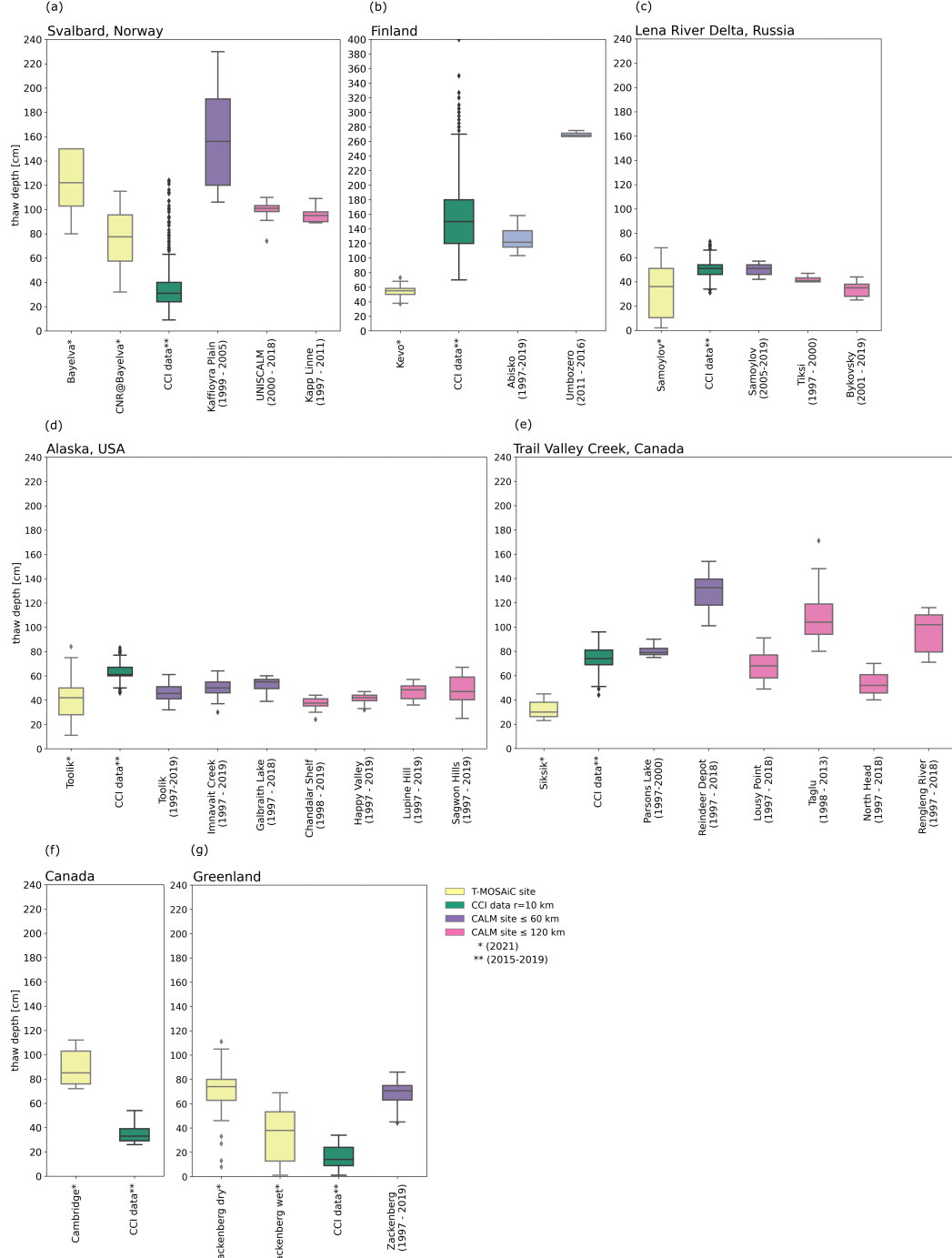


**Figure A6.** Comparison of the T-MOSAIc 2021 myThaw dataset (Martin et al., 2023) with the output from the ESA Permafrost Climate Change Initiative (Obu et al., 2021a) end-of season ALT product from 2015 to 2019 for all eight sites and the CALM ALT data (Heim et al., 2021). The Permafrost\_cci ALT output was investigated for a 10 km radius around each of the eight T-MOSAIc stations (Fig. 8, except for the two Bayelva sites (a) and the two Zackenberg transects (g) where one model ALT output was generated due to close proximity of the site locations (green box-plots). The purple box-plots contain the end-of-season ALT data obtained at the CALM sites in a 60 km radius around the T-MOSAIc sites. The pink box-plots contain the end-of-season ALT data obtained at the CALM sites in a 120 km radius around the T-MOSAIc sites.

**Table A1.** Summary table of the updated SACHI dataset, showing potential future infrastructure loss by coastal erosion, and estimated permafrost warming at infrastructure extent.

| Coastal region                      | n° of settlements | roads (km)  |       |         |       |           |        | other (km <sup>2</sup> ) |      |          |      | Infrastructure loss from coastal erosion (km <sup>2</sup> ) |      |       |      | Permafrost change at infrastructures |      |       |  |
|-------------------------------------|-------------------|-------------|-------|---------|-------|-----------|--------|--------------------------|------|----------|------|---|------|-------|------|--------------------------------------|------|-------|--|
|                                     |                   | dirt        |       | asphalt |       | undefined |        | buildings                |      | airstrip |      | water reservoir   |      | other |      | 2030                                 |      | 2050  |  |
|                                     |                   | settlements |       | roads   |       | roads     |        | roads                    |      | roads    |      | roads   |      | roads |      | roads                                |      | roads |  |
| Alaska (U.S)                        | 88                | 4127        | 2248  | 800     | 9     | 1.4       | 7      | 62                       | 1,9  | 2,6      | 4,8  | 0,99  | 2,97 | 7,93  | 0,1  | 0,31                                 | 0,83 |       |  |
| Canada                              | 87                | 5822        | 1623  | 3352    | 38    | 1.4       | 82     | 109                      | 0,08 | 0,8      | 0,1  | 0,4   | 0,73 | 1,18  | 0,04 | 0,13                                 | 0,34 |       |  |
| Greenland (Denmark)                 | 74                | -           | -     | -       | 8     | 0.3       | 0.2    | 36                       | -    | -        | -    | 0.1   | 0.31 | 0.83  | 0.03 | 0.09                                 | 0.25 |       |  |
| Svalbard (Norway)                   | 5                 | 106         | 119   | 10676   | 3.8   | 0.2       | 0.09   | 4                        | 0,4  | 0,4      | 1    | 1,19  | 3,58 | 9,54  | 0,04 | 0,12                                 | 0,32 |       |  |
| Russia                              | 154               | 18055       | 9413  | 32      | 62    | 3         | 47     | 412                      | 8,8  | 9,5      | 10   | 1,04  | 3,12 | 8,32  | 0,12 | 0,37                                 | 0,98 |       |  |
| Total (permafrost dominated coasts) | 408               | 28110       | 13403 | 14860   | 120.8 | 6.3       | 136.29 | 623                      | 11   | 12       | 17,8 | 0,90  | 2,70 | 7,20  | 0,10 | 0,31                                 | 0,83 |       |  |



## Open Research Section

The data that support the findings of this study will be openly available following an embargo at Zenodo. This study and associated datasets were designed for scientific purposes only and should not be taken as professional engineering advice.

## Acknowledgments

The project has received funding by the European Space Agency Polar Science Cluster Program Project EO4PAC. Further funding was received under the European Union's Horizon 2020 Research and Innovation Program under Grant Agreement No. 773421 for the Nunataryuk project. Further support was received by ESA CCI+ Permafrost. We acknowledge the use of Copernicus Sentinel data in this research. We acknowledge the use of Landsat data provided by the U.S. Geological Survey (USGS) in this research. Pléiades imagery was acquired through the ISIS Pléiades Program in connection with the WMO Polar Space Task Group. In-situ data was collected from drone surveys by the polar research group of the University of Lisbon.

## References

- Bartsch, A., Ley, S., Nitze, I., Pointner, G., & Vieira, G. (2020). Feasibility study for the application of synthetic aperture radar for coastal erosion rate quantification across the arctic. *Frontiers in Environmental Science*, 8, 143. doi: 10.3389/fenvs.2020.00143
- Bartsch, A., Pointner, G., Ingeman-Nielsen, T., & Lu, W. (2020). Towards circumpolar mapping of arctic settlements and infrastructure based on sentinel-1 and sentinel-2. *Remote Sensing*, 12(15), 2368. Retrieved from <https://www.mdpi.com/2072-4292/12/15/2368> doi: 10.3390/rs12152368
- Bartsch, A., Pointner, G., Nitze, I., Efimova, A., Jakober, D., Ley, S., ... Schweitzer, P. (2021). Expanding infrastructure and growing anthropogenic impacts along arctic coasts. *Environmental Research Letters*, 16(11), 115013. doi: 10.1088/1748-9326/ac3176
- Bartsch, A., Strozzi, T., & Nitze, I. (2023). Permafrost monitoring from space. *Surveys in Geophysics*, 1579–1613. doi: 10.1007/s10712-023-09770-3
- Bendixen, M., Lønsmann Iversen, L., Anker Bjørk, A., Elberling, B., Westergaard-Nielsen, A., Overeem, I., ... others (2017). Delta progradation in greenland driven by increasing glacial mass loss. *Nature*, 550(7674), 101–104. doi: 10.1038/nature23873
- Bergstedt, H., Zwieback, S., Bartsch, A., & Leibman, M. (2018). Dependence of c-band backscatter on ground temperature, air temperature and snow depth in arctic permafrost regions. *Remote Sensing*, 10(1), 142. doi: 10.3390/rs10010142
- Boike, J., Chadburn, S., Martin, J., Zwieback, S., Althuizen, I. H., Anselm, N., ... others (2021). Standardized monitoring of permafrost thaw: a user-friendly, multiparameter protocol. *Arctic Science*, 8(1), 153–182. doi: 10.1139/as-2021-0007
- Box, J. E., Hubbard, A., Bahr, D. B., Colgan, W. T., Fettweis, X., Mankoff, K. D., ... Fausto, R. S. (2022). Greenland ice sheet climate disequilibrium and committed sea-level rise. *Nature Climate Change*, 12(9), 808–813. Retrieved 2023-02-14, from <https://www.nature.com/articles/s41558-022-01441-2> doi: 10.1038/s41558-022-01441-2
- Buzard, R., Turner, M., Miller, K., Antrobus, D., & Overbeck, J. (2021). *Erosion exposure assessment of infrastructure in alaska coastal communities* (No. RI 2021-3). Retrieved 2023-02-14, from <http://www.dggs.alaska.gov/pubs/id/30672> doi: 10.14509/30672
- Crawford, A., Stroeve, J., Smith, A., & Jahn, A. (2021). Arctic open-water periods are projected to lengthen dramatically by 2100. *Communications Earth & Environment*, 2(1), 109. doi: 10.1038/s43247-021-00183-x

- Crawford, A. D., Lukovich, J. V., McCrystall, M. R., Stroeve, J. C., & Barber, D. G. (2022). Reduced sea ice enhances intensification of winter storms over the arctic ocean. *Journal of Climate*, 35(11), 3353–3370. doi: 10.1175/JCLI-D-21-0747.1
- Cunliffe, A. M., Tanski, G., Radosavljevic, B., Palmer, W. F., Sachs, T., Lantuit, H., ... Myers-Smith, I. H. (2019). Rapid retreat of permafrost coastline observed with aerial drone photogrammetry. *The Cryosphere*, 13(5), 1513–1528. doi: 10.5194/tc-13-1513-2019
- Ehrich, D., Thuestad, A. E., Tømmervik, H., Fauchald, P., & Hausner, V. H. (2019). Local land use associated with socio-economic development in six arctic regions. *Ambio*, 48, 649–660. doi: 10.1007/s13280-018-1095-y
- Gibbs, A., Jones, B., & Richmond, B. (2020). *A gis compilation of vector shorelines and coastal bluff edge positions, and associated rate-of-change data for barter island, alaska*. USGS, Pacific Coastal and Marine Science Center. doi: 10.5066/P9CRBC5I
- Glotov, V. E., Chlachula, J., Glotova, L. P., & Little, E. (2018). Causes and environmental impact of the gold-tailings dam failure at karamken, the russian far east. *Engineering Geology*, 245, 236–247. doi: 10.1016/j.enggeo.2018.08.012
- Grosse, G., Jones, B. M., & Arp, C. D. (2013). Thermokarst lakes, drainage, and drained basins. *Treatise on Geomorphology*, 8, 325–353. doi: 10.1016/B978-0-12-374739-6.00216-5
- Heim, B., Lisovski, S., Wieczorek, M., Pellet, C., Delaloye, R., Bartsch, A., ... Seifert, F. M. (2021). *D4.1 products validation and intercomparison report (pvir)*. Retrieved 2023-02-14, from [https://climate.esa.int/media/documents/CCI\\_PERMA\\_PVIR\\_v3.0\\_20210930.pdf](https://climate.esa.int/media/documents/CCI_PERMA_PVIR_v3.0_20210930.pdf)
- Hjort, J., Streletskiy, D., Doré, G., Wu, Q., Bjella, K., & Luoto, M. (2022). Impacts of permafrost degradation on infrastructure. *Nature Reviews Earth & Environment*, 3(1), 24–38.
- Ingeman-Nielsen, T., & Vakulenko, I. (2018). *Calibration and validation data for infratructure mapping, greenland, link to files*. doi: 10.1594/PANGAEA.895949
- IPCC. (2022). *The ocean and cryosphere in a changing climate: Special report of the intergovernmental panel on climate change* (1st ed.). Cambridge University Press. Retrieved from <https://www.cambridge.org/core/product/identifier/9781009157964/type/book> doi: 10.1017/9781009157964
- Irrgang, A. M., Bendixen, M., Farquharson, L. M., Baranskaya, A. V., Erikson, L. H., Gibbs, A. E., ... others (2022). Drivers, dynamics and impacts of changing arctic coasts. *Nature Reviews Earth & Environment*, 3(1), 39–54. doi: doi.org/10.1038/s43017-021-00232-1
- Irrgang, A. M., Lantuit, H., Manson, G. K., Günther, F., Grosse, G., & Overduin, P. P. (2018). Variability in rates of coastal change along the yukon coast, 1951 to 2015. *Journal of Geophysical Research: Earth Surface*, 123(4), 779–800. doi: 10.1002/2017JF004326
- Isaev, V., Koshurnikov, A., Pogorelov, A., Amangurov, R., Podchasov, O., Sergeev, D., ... Kioka, A. (2019). Cliff retreat of permafrost coast in south-west baydaratskaya bay, kara sea, during 2005–2016. *Permafrost and Periglacial Processes*, 30(1), 35–47. doi: 10.1002/ppp.1993
- Jones, B., Irrgang, A., Farquharson, L., Lantuit, H., Whalen, D., Ogorodov, S., ... others (2020). Arctic report card 2020: coastal permafrost erosion. *NOAA Institutional Repository*. doi: 10.25923/e47w-dw52
- Jones, B. M., Farquharson, L. M., Baughman, C. A., Buzard, R. M., Arp, C. D., Grosse, G., ... others (2018). A decade of remotely sensed observations highlight complex processes linked to coastal permafrost bluff erosion in the arctic. *Environmental Research Letters*, 13(11), 115001. doi: 10.1088/1748-9326/aae471
- Kumar, D. (2021). Urban objects detection from c-band synthetic aperture radar (sar) satellite images through simulating filter properties. *Scientific Reports*, 11(1), 6241. doi: 10.1038/s41598-021-85121-9
- Langer, M., von Deimling, T. S., Westermann, S., Rolph, R., Rutte, R., Antonova, S., ...



- Grosse, G. (2023). Thawing permafrost poses environmental threat to thousands of sites with legacy industrial contamination. *Nature Communications*, 14(1), 1721. doi: [oi.org/10.1038/s41467-023-37276-4](https://doi.org/10.1038/s41467-023-37276-4)
- Lantuit, H., Overduin, P. P., Couture, N., Wetterich, S., Aré, F., Atkinson, D., ... others (2012). The arctic coastal dynamics database: A new classification scheme and statistics on arctic permafrost coastlines. *Estuaries and Coasts*, 35, 383–400.
- Liljedahl, A. K., Boike, J., Daanen, R. P., Fedorov, A. N., Frost, G. V., Grosse, G., ... others (2016). Pan-arctic ice-wedge degradation in warming permafrost and its influence on tundra hydrology. *Nature Geoscience*, 9(4), 312–318. doi: 10.1038/ngeo2674
- Llano, X. (2022). *Acatama - qgis plugin for accuracy assessment of thematic maps*. Retrieved from <https://github.com/SMBYC/AcATaMa>
- Lu, W., Aalberg, A., Høyland, K., Lubbad, R., Løset, S., & Ingeman-Nielsen, T. (2018). *Calibration data for infratructure mapping in svalbard, link to files*. doi: 10.1594/PANGAEA.895950
- Luetzenburg, G., Townsend, D., Svennevig, K., Bendixen, M., Bjørk, A., Eidam, E., & Kroon, A. (2023). Sedimentary coastal cliff erosion in greenland. *Journal of Geophysical Research: Earth Surface*, e2022JF007026. doi: 10.1029/2022JF007026
- Malenfant, F., Whalen, D., Fraser, P., & van Proosdij, D. (2022). Rapid coastal erosion of ice-bonded deposits on pelly island, southeastern beaufort sea, inuvialuit settlement region, western canadian arctic. *Canadian Journal of Earth Sciences*, 59(11), 961–972. Retrieved from <https://cdnsiencepub.com/doi/10.1139/cjes-2021-0118> doi: 10.1139/cjes-2021-0118
- Marino, E., & Lazrus, H. (2015). Migration or forced displacement ?: the complex choices of climate change and disaster migrants in shishmaref, alaska and nanumea, tuvalu. *Human Organization*, 74(4), 341–350. doi: 10.17730/0018-7259-74.4.341
- Martin, J., Boike, J., Chadburn, S., Zwieback, S., Anselm, N., Goldau, M. P., ... Young, A. (2023). *T-mosaic 2021 mythaw data set*. PANGAEA. Retrieved from <https://doi.org/10.1594/PANGAEA.956039> doi: 10.1594/PANGAEA.956039
- Meredith, M., Sommerkorn, M., Cassotta, S., Derksen, C., Ekaykin, A., Hollowed, A., ... others (2019). *Polar regions. chapter 3, ipcc special report on the ocean and cryosphere in a changing climate*.
- Miner, K. R., Turetsky, M. R., Malina, E., Bartsch, A., Tamminen, J., McGuire, A. D., ... Miller, C. E. (2022). Permafrost carbon emissions in a changing arctic. *Nature Reviews Earth & Environment*, 3(1), 55–67. doi: 10.1038/s43017-021-00230-3
- Nicu, I. C., Rubensdotter, L., Stalsberg, K., & Nau, E. (2021). Coastal erosion of arctic cultural heritage in danger: A case study from svalbard, norway. *Water*, 13(6), 784. doi: 10.3390/w13060784
- Nielsen, D. M., Pieper, P., Barkhordarian, A., Overduin, P., Ilyina, T., Brovkin, V., ... Dobrynin, M. (2022). Increase in arctic coastal erosion and its sensitivity to warming in the twenty-first century. *Nature Climate Change*, 12(3), 263–270. Retrieved 2023-02-14, from <https://www.nature.com/articles/s41558-022-01281-0> doi: 10.1038/s41558-022-01281-0
- Nitze, I., Grosse, G., Jones, B. M., Arp, C. D., Ulrich, M., Fedorov, A., & Veremeeva, A. (2017). Landsat-based trend analysis of lake dynamics across northern permafrost regions. *Remote Sensing*, 9(7), 640. doi: 10.3390/rs9070640
- Obu, J., Westermann, S., Barboux, C., Bartsch, A., Delaloye, R., Grosse, G., ... Wiesmann, A. (2021a). *ESA Permafrost Climate Change Initiative (permafrost\_cci): Permafrost active layer thickness for the Northern Hemisphere, v3.0*. CEDA. Centre for Environmental Data Analysis (CEDA). Retrieved from <https://catalogue.ceda.ac.uk/uuid/67a3f8c8dc914ef99f7f08eb0d997e23> doi: 10.5285/29C4AF5986BA4B9C8A3CFC33CA8D7C85
- Obu, J., Westermann, S., Barboux, C., Bartsch, A., Delaloye, R., Grosse, G., ... Wiesmann, A. (2021b). *ESA Permafrost Climate Change Initiative (permafrost\_cci): Permafrost ground temperature for the Northern Hemisphere, v3.0*. CEDA. Centre for Environmental Data Analysis (CEDA). Retrieved from <https://>

- catalogue.ceda.ac.uk/uuid/b25d4a6174de4ac78000d034f500a268 doi: 10.5285/b25d4a6174de4ac78000d034f500a268
- Obu, J., Westermann, S., Barboux, C., Bartsch, A., Delaloye, R., Grosse, G., ... others (2021c). *Permafrost extent for the northern hemisphere, v3.0., centre for environmental data analysis [data set]*. doi: 10.5285/6e2091cb0c8b4106921b63cd5357c97c
- Ogorodov, S., Alekseyutina, D., Baranskaya, A., Shabanova, N., & Shilova, O. (2020). Coastal erosion of the russian arctic: An overview. *Journal of Coastal Research*, 95(SI), 599–604. doi: 10.2112/SI95-117.1
- Ogorodov, S., Badina, S., & Bogatova, D. (2023). Sea coast of the western part o the russian arctic under climate change: Dynamics, technogenic influence and potential economic damage. *Climate*, 11(7), 143. doi: 10.3390/cli11070143
- Oppenheimer, M., Glavovic, B., Hinkel, J., van de Wal, R., Magnan, A. K., Abd-Elgawad, A., ... others (2019). Sea level rise and implications for low lying islands, coasts and communities. *IPCC Special Report on the Ocean and Cryosphere in a Changing Climate..* doi: 10.1017/9781009157964.006.
- Overduin, P. P., Strzelecki, M. C., Grigoriev, M. N., Couture, N., Lantuit, H., St-Hilaire-Gravel, D., ... Wetterich, S. (2014). Coastal changes in the arctic. *Geological Society, London, Special Publications*, 388(1), 103–129. Retrieved 2023-02-14, from <https://www.lyellcollection.org/doi/10.1144/SP388.13> doi: 10.1144/SP388.13
- Overeem, I., Anderson, R. S., Wobus, C. W., Clow, G. D., Urban, F. E., & Matell, N. (2011). Sea ice loss enhances wave action at the arctic coast. *Geophysical Research Letters*, 38(17). doi: 10.1029/2011GL048681
- Palmtag, J., Obu, J., Kuhry, P., Richter, A., Siewert, M. B., Weiss, N., ... Hugelius, G. (2022). A high spatial resolution soil carbon and nitrogen dataset for the northern permafrost region based on circumpolar land cover upscaling. *Earth System Science Data*, 14(9), 4095–4110. doi: 10.5194/essd-14-4095-2022
- Radosavljevic, B., Lantuit, H., Pollard, W., Overduin, P., Couture, N., Sachs, T., ... Fritz, M. (2016). Erosion and flooding—threats to coastal infrastructure in the arctic: a case study from herschel island, yukon territory, canada. *Estuaries and Coasts*, 39, 900–915. doi: 10.1007/s12237-015-0046-0
- Rose, S. K., Andersen, O. B., Passaro, M., Ludwigsen, C. A., & Schwatke, C. (2019). Arctic ocean sea level record from the complete radar altimetry era: 1991–2018. *Remote Sensing*, 11(14), 1672. Retrieved 2023-02-14, from <https://www.mdpi.com/2072-4292/11/14/1672> doi: 10.3390/rs11141672
- Smith, S. L., O'Neill, H. B., Isaksen, K., Noetzli, J., & Romanovsky, V. E. (2022). The changing thermal state of permafrost. *Nature Reviews Earth & Environment*, 3(1), 10–23. doi: 10.1038/s43017-021-00240-1
- Solomon, S. M. (2005). Spatial and temporal variability of shoreline change in the beaufort-mackenzie region, northwest territories, canada. *Geo-Marine Letters*, 25(2-3), 127–137. doi: 10.1007/s00367-004-0194-x
- Streletskiy, D., & Shiklomanov, N. (2021). *Circum polar active layer monitoring (calm)*. Retrieved from <https://arcticdata.io/catalog> (data retrieved from Arctic Data Center)
- Streletskiy, D. A., Suter, L. J., Shiklomanov, N. I., Porfiriev, B. N., & Eliseev, D. O. (2019a). Assessment of climate change impacts on buildings, structures and infrastructure in the russian regions on permafrost. *Environmental Research Letters*, 14(2), 025003. doi: 10.1088/1748-9326/aaf5e6
- Streletskiy, D. A., Suter, L. J., Shiklomanov, N. I., Porfiriev, B. N., & Eliseev, D. O. (2019b). Assessment of climate change impacts on buildings, structures and infrastructure in the russian regions on permafrost. *Environmental Research Letters*, 14(2), 025003. doi: 10.1088/1748-9326/aaf5e6
- Stroeve, J., & Notz, D. (2018). Changing state of arctic sea ice across all seasons. *Environmental Research Letters*, 13(10), 103001. doi: 10.1088/1748-9326/aade56
- Strozzi, T., Antonova, S., Günther, F., Mätzler, E., Vieira, G., Wegmüller, U., ... Bartsch, A. (2018). Sentinel-1 sar interferometry for surface deformation monitoring in low-land

- permafrost areas. *Remote Sensing*, 10(9), 1360. doi: 10.3390/rs10091360
- Tanguy, R., Whalen, D., Prates, G., Pina, P., Freitas, P., Bergstedt, H., & Vieira, G. (2023). Permafrost degradation in the ice-wedge tundra terrace of paulatuk peninsula (darnley bay, canada). *Geomorphology*, 108754. doi: 10.1016/j.geomorph.2023.108754
- Tanguy, R., Whalen, D., Prates, G., & Vieira, G. (2023). Shoreline change rates and land to sea sediment and soil organic carbon transfer in eastern parry peninsula from 1965 to 2020 (amundsen gulf, canada). *Arctic Science*. doi: 10.1139/AS-2022-0028
- Thieler, E. R., Himmelstoss, E. A., Zichichi, J. L., & Ergul, A. (2009). *The digital shoreline analysis system (dsas) version 4.0-an arcgis extension for calculating shoreline change* (Tech. Rep.). US Geological Survey. doi: 10.3133/ofr20081278
- Thomas, M. A., Mota, A., Jones, B. M., Choens, R. C., Frederick, J. M., & Bull, D. L. (2020). Geometric and material variability influences stress states relevant to coastal permafrost bluff failure. *Frontiers in Earth Science*, 8, 143. doi: 10.3389/feart.2020.00143
- Vasiliev, A. A., Drozdov, D. S., Gravis, A. G., Malkova, G. V., Nyland, K. E., & Streletskiy, D. A. (2020). Permafrost degradation in the western russian arctic. *Environmental Research Letters*, 15(4), 045001. doi: 10.1088/1748-9326/ab6f12
- Wagner, A. M., Lindsey, N. J., Dou, S., Gelvin, A., Saari, S., Williams, C., . . . others (2018). Permafrost degradation and subsidence observations during a controlled warming experiment. *Scientific reports*, 8(1), 10908. doi: 10.1038/s41598-018-29292-y
- Westermann, S., Østby, T., Gislås, K., Schuler, T., & Etzelmüller, B. (2015). A ground temperature map of the north atlantic permafrost region based on remote sensing and reanalysis data. *The Cryosphere*, 9(3), 1303–1319. doi: 10.5194/tc-9-1303-2015
- Whalen, D., Forbes, D., Kostylev, V., Lim, M., Fraser, P., Nedimović, M., & Stuckey, S. (2022). Mechanisms, volumetric assessment, and prognosis for rapid coastal erosion of tuktoyaktuk island, an important natural barrier for the harbour and community. *Canadian Journal of Earth Sciences*, 59(11), 945–960. doi: 10.1139/cjes-2021-0101
- Xu, N. (2018). Detecting coastline change with all available landsat data over 1986–2015: A case study for the state of texas, usa. *Atmosphere*, 9(3), 107. doi: 10.3390/atmos9030107